



RESEARCH ARTICLE

10.1002/2015WR018450

Key Points:

- Adaptive mixed finite element method is proposed for simulation of Darcy flow in fractured porous media
- A novel residual type of a posteriori error estimator is introduced
- An efficient upscaling algorithm is proposed to compute the effective permeability of the fractured porous media

Correspondence to:

S. Sun,
shuyu.sun@kaust.edu.sa

Citation:

Chen, H., A. Salama, and S. Sun (2016), Adaptive mixed finite element methods for Darcy flow in fractured porous media, *Water Resour. Res.*, 52, 7851–7868, doi:10.1002/2015WR018450.

Received 2 DEC 2015

Accepted 17 SEP 2016

Accepted article online 21 SEP 2016

Published online 12 OCT 2016

Adaptive mixed finite element methods for Darcy flow in fractured porous media

Huangxin Chen^{1,2}, Amgad Salama³, and Shuyu Sun²

¹School of Mathematical Sciences and Fujian Provincial Key Laboratory on Mathematical Modeling and High Performance Scientific Computing, Xiamen University, Fujian, China, ²Computational Transport Phenomena Laboratory, Division of Physical Science and Engineering, King Abdullah University of Science and Technology, Thuwal, Saudi Arabia, ³Reservoir Engineering Research Institute, Palo Alto, California, USA

Abstract In this paper, we propose adaptive mixed finite element methods for simulating the single-phase Darcy flow in two-dimensional fractured porous media. The reduced model that we use for the simulation is a discrete fracture model coupling Darcy flows in the matrix and the fractures, and the fractures are modeled by one-dimensional entities. The Raviart-Thomas mixed finite element methods are utilized for the solution of the coupled Darcy flows in the matrix and the fractures. In order to improve the efficiency of the simulation, we use adaptive mixed finite element methods based on novel residual-based a posteriori error estimators. In addition, we develop an efficient upscaling algorithm to compute the effective permeability of the fractured porous media. Several interesting examples of Darcy flow in the fractured porous media are presented to demonstrate the robustness of the algorithm.

1. Introduction

Modeling of fluid flow in fractured porous media has become a significant problem due to its application in many of the environmental and energy problems. Various models which include the discrete fracture model (DFM), the dual porosity model, and some improvements have been studied by a number of authors [see, e.g., Barenblatt *et al.*, 1960; Warren and Root, 1963; Baca *et al.*, 1984; Noorishad and Mehra, 1982; Alboin *et al.*, 2002; Frih *et al.*, 2008; Martin *et al.*, 2005; Hoteit and Firoozabadi, 2005; Pruess and Narasimhan, 1985; Wu and Pruess, 1988; Zidane and Firoozabadi, 2014; Dong *et al.*, 2011; Song and Sun, 2012; Cai and Sun, 2013, and references therein]. For example, in highly fractured rock mass, an equivalent porous medium may replace the rock system. In moderately fractured rock system, a framework based on a number of overlapping continua may be established (e.g., dual porosity and dual permeability models). In domains where there exist a relatively smaller number of fractures, it may be possible to incorporate the fractures with the main domain and impose different properties to the fractures domains. Apparently, this approach requires denser mesh to resolve the fracture region when solving the governing equations numerically. Another approach, named the DFM (or reduced model), in which the fractures are dealt with as lower dimensionality surfaces in the computational domain. In this work, we are interested in the reduced model based on the DFM approach in which there is communication between the fractures and the surrounding matrix blocks.

Two types of fractures usually appear in the porous media. The first type called conductors which are much more permeable than that in the surrounding matrix block, and the second type called barriers which are less permeable than that in the surrounding matrix block. For both types of fractures, the reduced models have been presented for single-phase Darcy flow [Alboin *et al.*, 2002; Frih *et al.*, 2008; Martin *et al.*, 2005] where the fracture flow equations and the proper interface conditions across the reduced fractures have been addressed. Lots of numerical methods based on the DFM have been utilized to simulate fluid flow in fractured porous media, such as finite difference methods, finite volume methods and finite element methods [see, e.g., Hoteit and Firoozabadi, 2008] and the references therein. In this paper, we use the mixed finite element methods to solve the reduced model of coupled Darcy flow in fractured porous media. In order to improve the efficiency of simulation, we apply the adaptivity methodology to better capture the potential singularities of the solution. For the adaptive refinement of the mesh in a loop of the AMFEM, we use the a posteriori error estimators. One can refer to Carstensen [1997], Larson and Maqvist [2008], and Lovadina and Stenberg [2006] for the a posteriori error estimators for the mixed finite element methods, Du *et al.* [2016]

for the a posteriori error estimators for the multipoint flux mixed finite element methods, and *Carstensen and Hoppe* [2006] and *Chen et al.* [2010] for convergence analysis of the AMFEM. In this work, we will utilize the residual-based a posteriori error estimators for the mixed finite element methods based on the DFM.

For the DFM, the grid should be generated according to the geometry and locations of fractures such that the grid cell for fractures are located at the matrix cell interface. The extended finite element method (XFEM) was applied in *Fumagalli* [2012], *D'Angelo and Scotti* [2012], *Formaggia et al.* [2014], and *Schwenck* [2015] to avoid generating complex conforming grid. The property of the XFEM that the matrix grid and the fracture grid can be nonmatching at the intersection is an advantage of this approach. Compared with the DFM, the finite element spaces used in the XFEM should be enriched by the finite element basis on the elements cut by the fractures with discontinuous functions. In this paper, we further apply the AMFEM in the DFM to improve the quality of numerical approximation. Another approach, the embedded discrete fracture model (EDFM) was introduced by *Lee et al.* [2000, 2001] and *Li and Lee* [2008] to simulate the flow in fractured porous media by a hierarchical fracture modeling. The small-scale fractures are homogenized, while the long fractures are treated as low-dimensional objects and the flux interaction between fractures and matrix are dealt with as a source term. The EDFM can avoid using complex grid for matrix-fracture system compared with the DFM. Some applications of the EDFM in the multiscale approach were introduced in *Hajibeygi et al.* [2011] for iterative multiscale finite volume method and in *Efendiev et al.* [2015] for generalized multiscale finite element method. A comparison of the DFM, the EDFM, and the dual-permeability approach was shown in *Moinfar et al.* [2011]. We also mention that the continuum flow models accounting for two scales were developed in *Karimi-Fard et al.* [2006] and *Karimi-Fard and Durlofsky* [2014]. It can reduce a total number of degrees of freedom in the model without significant loose in accuracy. This technique coupled with a multicontinuum approach provides a possibility to capture all important transient scales in a coarse model. Moreover, the authors in *Karimi-Fard and Durlofsky* [2014] used the hierarchical grid based on the adaptive methodology as the simulation grid which facilitates the efficient simulation. We denote by N_e the number of elements in the grid which can be used to simulate the fluid flow in the fractured porous media and N_f the number of fractures. We focus on the case $N_e \gg N_f$ which can be modeled by the DFM, and in this case the complexity of the proposed method based on the AMFEM increases only slightly as the number of fractures increases. For the case $N_e \approx N_f$, in particular, when lots of fractures exist in the whole domain in complex configurations with multiple length scales, the multiscale method may be applied.

The effective permeability on the coarse scale is an interesting topic for the fractured porous media block. Some upscaling techniques were developed to calculate effective permeability for fracture reservoir [see *Oda*, 1985; *Durlofsky*, 1991; *Lough et al.*, 1997; *Nakashima et al.*, 2001, and the references therein]. Compared with the algorithms in literature, our algorithm for effective permeability is developed by the flow-based upscaling technique based on the reduced model [cf. *Martin et al.*, 2005] and can be used for the conductive or barrier fracture system. Different from *Karimi-Fard and Durlofsky* [2014], we focus on only a fractured porous media block to calculate the effective permeability; thus, we construct a quasi-uniform conforming coarsest grid, and the AMFEM can be utilized for the simulation of the problem on the fractured porous media block.

To test the efficiency of the AMFEM for the reduced model of Darcy flow in fractured porous media, we carry out four interesting examples for simulation. The first example is to compute the effective permeability of the whole fractured porous media and test how the fractures of certain assignment can affect the anisotropic flow in a larger scale. The effective permeability of the entire porous media is computed, which is expected to be anisotropic due to the fractures even though individual matrix blocks or fractures are isotropic. The second example is to test the problems where the globally imposed pressure gradient tends to drive the fluid in a single direction, but in a local area the fluid may flow backward because of the fracture with large permeability which connects the inflow boundary and the outflow boundary. The third example is to test the problem of short-cut flow where the fracture interacts with high-permeable and low-permeable zones, which indicates the effect and significance of the fracture. The fourth example is to test the problem with a number of fractures which satisfy a certain distribution, and to study the trend of flow behavior with fracture distribution parameters.

The paper is organized as follows: in section 2, we introduce some notations, the reduced model of coupled Darcy flows in fractured porous media and the associated Raviart-Thomas mixed finite element approximation. The a posteriori error estimators are presented in section 3 and the approach to compute the effective

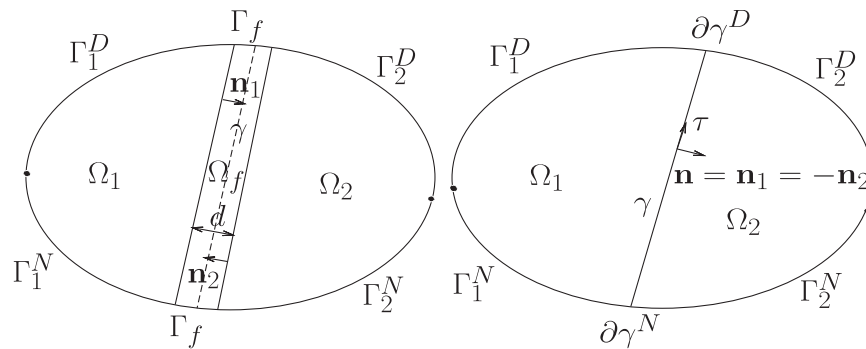


Figure 1. (left) The domain Ω with a single fracture subdomain Ω_f , (right) The subdomains Ω_1 , Ω_2 and the reduced fracture γ .

permeability of fractured porous media is given in section 4. In section 5, we present some numerical experiments for simulations of the reduced model for flow in fractured porous media and verifying the robustness of the AMFEM. The paper is finally concluded in section 6.

2. The Model and Mixed Finite Element Approximation

2.1. Notations and the Model

Let $\Omega \in \mathbb{R}^2$ be a bounded and simply connected porous media domain with Lipschitz continuous boundary. For low-velocity flow in which inertial effect is neglected, the single-phase flow in Ω governed by mass conservation and Darcy's law can be written as:

$$\nabla \cdot \mathbf{u} = q \quad \text{in } \Omega, \quad (1a)$$

$$\mathbf{u} = -\mathbf{K} \nabla p \quad \text{in } \Omega, \quad (1b)$$

where p is the pressure, \mathbf{u} is the Darcy velocity, \mathbf{K} is a bounded symmetric and positive definite permeability tensor, and q is the source term. We will assume Dirichlet boundary condition and Neumann boundary condition are both imposed on parts of $\partial\Omega$.

We will utilize the reduced model proposed in *Martin et al.* [2005] based on the DFM to describe the flow in the fracture as a lower dimensional problem. The fracture Ω_f is assumed to be a thin subdomain of Ω with permeability different from the surrounding matrix block. For simplicity, we assume that there is a single fracture subdomain in the porous media and the domain Ω is separated into three connected subdomains Ω_1 , Ω_2 , and Ω_f as shown in the left graph of Figure 1. We assume that the fracture domain Ω_f may be written as $\Omega_f = \{x \in \Omega : x = s + t\mathbf{n}, s \in \gamma \text{ and } t \in (-\frac{d(s)}{2}, \frac{d(s)}{2})\}$, where γ is a one-dimensional polygonal line, $\mathbf{n} = \mathbf{n}_1 = -\mathbf{n}_2$ is the unit normal vector to γ , $\mathbf{n}_{i=1,2}$ is the unit normal on $\partial\Omega_i \cap \partial\Omega_f$ outward with respect to Ω_i , and $d(s)$ denotes the thickness of fracture at the point $s \in \gamma$. We assume that the permeability tensor is bounded, symmetric and positive definite in the matrix block subdomains Ω_1 , Ω_2 and is denoted by \mathbf{K}_i in Ω_i for $i = 1, 2$. The permeability tensor \mathbf{K}_f in Ω_f is assumed to be split into a tangential part $\mathbf{K}_{f,\tau}$ and a normal part $\mathbf{K}_{f,n}$ as $\mathbf{K}_f = \text{diag}(\mathbf{K}_{f,\tau}, \mathbf{K}_{f,n})$. Let τ be the unit tangential vector to γ . Here we denote by $\text{diag}(a, b)$ a 2×2 diagonal matrix with the elements of $[a, b]$ on the main diagonal. We always assume $(\mathbf{K}_f \tau, \mathbf{n}) = 0$ throughout the paper.

We denote by ∇_τ and $\nabla_\tau \cdot$ the tangential gradient and divergence operators along γ . For the domain shown in the right graph of Figure 1 for the reduced model, we denote by Γ_i^D and Γ_i^N the Dirichlet and Neumann boundary, respectively, in the subdomain Ω_i , $i = 1, 2$. The ends of γ are denoted by $\partial\gamma^D$ and $\partial\gamma^N$ the Dirichlet and Neumann boundary, respectively, for the reduced flow model on γ . Let \mathbf{u}_i, p_i, q_i be the restrictions of \mathbf{u}, p, q in Ω_i for $i = 1, 2, f$. We denote by $\{\cdot\}_\gamma$ the average of a quantity on γ such that $\{\psi\}_\gamma = \frac{1}{2}(\psi|_\gamma + \psi|_\gamma)$ and $[[\psi]]_\gamma$ the jump of a quantity across γ such that $[[\psi]]_\gamma = \psi|_\gamma - \psi|_\gamma$, where $\psi|_{i=1,2}$ is a function defined in Ω_i with well-defined trace on γ . By averaging the conservation equation ((1a)a) and the Darcy's law (1b) over cross section of the fracture Ω_f , the reduced model within the domain in the right graph of Figure 1 can be written as [cf. *Martin et al.*, 2005]:

$$\nabla \cdot \mathbf{u}_i = q_i \quad \text{in } \Omega_i, i = 1, 2, \quad (2a)$$

$$\mathbf{u}_i = -\mathbf{K}_i \nabla p_i \quad \text{in } \Omega_i, \quad i=1, 2, \quad (2b)$$

together with the reduced equations

$$\nabla_{\tau} \cdot \hat{\mathbf{u}}_{\gamma} = \hat{q}_{\gamma} + \llbracket \mathbf{u} \cdot \mathbf{n} \rrbracket_{\gamma} \quad \text{on } \gamma, \quad (2c)$$

$$\hat{\eta}_{\gamma} \hat{\mathbf{u}}_{\gamma} + \nabla_{\tau} \hat{p}_{\gamma} = 0 \quad \text{on } \gamma, \quad (2d)$$

and the interface conditions

$$\xi_{\gamma} \eta_{\gamma} \llbracket \mathbf{u} \cdot \mathbf{n} \rrbracket_{\gamma} = \{p\}_{\gamma} - \hat{p}_{\gamma} \quad \text{on } \gamma, \quad (2e)$$

$$\eta_{\gamma} \{\mathbf{u} \cdot \mathbf{n}\}_{\gamma} = \llbracket p \rrbracket_{\gamma}, \quad \text{on } \gamma, \quad (2f)$$

where $\hat{\mathbf{u}}_{\gamma} = \int_{-\frac{d(s)}{2}}^{\frac{d(s)}{2}} (\mathbf{u}_f(s, t) \cdot \boldsymbol{\tau}(s)) \boldsymbol{\tau}(s) dt$, $\hat{p}_{\gamma} = \frac{1}{d(s)} \int_{-\frac{d(s)}{2}}^{\frac{d(s)}{2}} p_f(s, t) dt$ and $\hat{q}_{\gamma} = \int_{-\frac{d(s)}{2}}^{\frac{d(s)}{2}} q_f(s, t) dt$. The boundary conditions are assumed to be $p_i = g_i^D$ on Γ_i^D , $\mathbf{u}_i \cdot \mathbf{n}_{\Gamma} = g_i^N$ on Γ_i^N , $i=1, 2$, and $\hat{p}_{\gamma} = \hat{g}_{\gamma}^D$ on $\partial\gamma^D$, $\hat{\mathbf{u}}_{\gamma} \cdot \boldsymbol{\tau} = \hat{g}_{\gamma}^N$ on $\partial\gamma^N$, where $g_i^D|_{i=1,2}$, \hat{g}_{γ}^D , \hat{g}_{γ}^N are boundary data, and \mathbf{n}_{Γ} is the unit outward normal on $\partial\Omega$. The parameters in (2e) and (2f) are defined as $\hat{\eta}_{\gamma}^{-1} = d(s) \mathbf{K}_{f,\tau}$, $\eta_{\gamma} = d(s) / \mathbf{K}_{f,n}$, and $\xi_{\gamma} = \frac{2\xi-1}{4}$, $\xi > 1/2$. Note that $\hat{\mathbf{u}}_{\gamma}$ simulates the tangential component of Darcy velocity along the reduced fracture γ , and the corresponding normal component $\hat{\mathbf{u}}_{\gamma}^n$ of Darcy velocity along γ can be directly obtained by $\hat{\mathbf{u}}_{\gamma}^n = \mathbf{K}_{f,n} \llbracket p \rrbracket_{\gamma} = d(s) \{\mathbf{u} \cdot \mathbf{n}\}_{\gamma}$. When the fractures are more permeable than that in the surrounding matrix blocks, the Neumann boundary condition on $\partial\gamma^N$, which is immersed in the porous media, can be considered as $\hat{\mathbf{u}}_{\gamma} \cdot \boldsymbol{\tau}|_{\partial\gamma^N} = 0$. Then, the reduced model can be extended to the problem with more reduced nonintersecting fractures which are nonimmersed, partially immersed or totally immersed in the porous media.

In the following, standard notations and definitions for Sobolev spaces [cf. Adams, 1975] are used throughout the paper. In order to introduce the weak formulation and its discrete version of the reduced model (2), we define the sets

$$\mathbf{u}_i^{g_i^N} = \{\mathbf{v}_i \in H(\text{div}, \Omega_i) : \mathbf{v}_i \cdot \mathbf{n}_{\Gamma} = g_i^N \text{ on } \Gamma_i^N, \mathbf{v}_i \cdot \mathbf{n}_i \in L^2(\gamma)\}, \quad i=1, 2,$$

$$\mathbf{u}_{\gamma}^{\hat{g}_{\gamma}^N} = \{\hat{\mathbf{v}}_{\gamma} \in [L^2(\gamma)]^2 : \hat{\mathbf{v}}_{\gamma} \cdot \mathbf{n} = 0, \nabla_{\tau} \cdot \hat{\mathbf{v}}_{\gamma} \in L^2(\gamma), \hat{\mathbf{v}}_{\gamma} \cdot \mathbf{n}_{\Gamma} = \hat{g}_{\gamma}^N\}.$$

Let $g^D = (g_1^D, g_2^D, \hat{g}_{\gamma}^D)$, $g^N = (g_1^N, g_2^N, \hat{g}_{\gamma}^N)$, $Q_1 = L^2(\Omega_1)$, $Q_2 = L^2(\Omega_2)$, $Q_{\gamma} = L^2(\gamma)$. We define $\mathbf{u}^{g^N} = \mathbf{u}_1^{g_1^N} \times \mathbf{u}_2^{g_2^N} \times \mathbf{u}_{\gamma}^{\hat{g}_{\gamma}^N}$ and $Q = Q_1 \times Q_2 \times Q_{\gamma}$ endowed with the product norms

$$\|\mathbf{v}^*\|_{\mathbf{u}}^2 = \sum_{i=1}^2 (\|\mathbf{v}_i\|_{0,\Omega_i}^2 + \|\nabla \cdot \mathbf{v}_i\|_{0,\Omega_i}^2) + \sum_{i=1}^2 \|\mathbf{v}_i \cdot \mathbf{n}\|_{0,\gamma}^2 + \|\hat{\mathbf{v}}_{\gamma}\|_{0,\gamma}^2 + \|\nabla_{\tau} \cdot \hat{\mathbf{v}}_{\gamma}\|_{0,\gamma}^2,$$

$$\|r^*\|_Q^2 = \sum_{i=1}^2 \|r_i\|_{0,\Omega_i}^2 + \|\hat{r}_{\gamma}\|_{0,\gamma}^2$$

for all $\mathbf{v}^* = (\mathbf{v}_1, \mathbf{v}_2, \hat{\mathbf{v}}_{\gamma}) \in \mathbf{u}^{g^N}$ and $r^* = (r_1, r_2, \hat{r}_{\gamma}) \in Q$.

Let \mathcal{T}_h^i be a conforming, shape-regular simplicial triangulation of Ω_i , $i=1, 2$, and \mathcal{T}_h^{γ} be the finite element partition of γ . We assume that \mathcal{T}_h^1 , \mathcal{T}_h^2 and \mathcal{T}_h^{γ} are matching at the interface γ . Now we introduce the well-known Raviart-Thomas mixed finite element space of order k as: $\text{RT}_k = [\mathbb{P}_k]^2 \oplus \mathbf{x} \mathbb{P}_k$, where \mathbb{P}_k is the polynomial space of degree $k \geq 0$. We define $\mathbf{u}_h^0 = \mathbf{u}_{1,h}^0 \times \mathbf{u}_{2,h}^0 \times \mathbf{u}_{\gamma,h}^0$ and $Q_h = Q_{1,h} \times Q_{2,h} \times Q_{\gamma,h}$, where

$$\mathbf{u}_{i,h}^0 = \{\mathbf{v}_i \in \mathbf{u}_i^0 : \mathbf{v}_i|_T \in \text{RT}_k(T), \forall T \in \mathcal{T}_h^i\}, \quad i=1, 2,$$

$$Q_{i,h} = \{r_i \in Q_i : r_i|_T \in \mathbb{P}_k(T), \forall T \in \mathcal{T}_h^i\}, \quad i=1, 2,$$

and

$$\mathbf{u}_{\gamma,h}^0 = \{\hat{\mathbf{v}}_{\gamma} \in \mathbf{u}_{\gamma}^0 : \hat{\mathbf{v}}_{\gamma}|_e \in \text{RT}_k(e), \forall e \in \mathcal{T}_h^{\gamma}\},$$

$$Q_{\gamma,h} = \{\hat{r}_{\gamma} \in Q_{\gamma} : \hat{r}_{\gamma}|_e \in \mathbb{P}_k(e), \forall e \in \mathcal{T}_h^{\gamma}\}.$$

2.2. Weak Formulation and Mixed Finite Element Approximation

In the following, we always assume $\Gamma_i^D|_{i=1,2} \neq \emptyset$, $\partial\gamma^D \neq \emptyset$ and $g^N=0$ if $\Gamma_i^N|_{i=1,2} \neq \emptyset$, $\partial\gamma^N \neq \emptyset$ for simplicity. Extension to nonhomogeneous Neumann boundary condition is straightforward. The weak formulation of the reduced model (2) can be written as: Find $(\mathbf{u}^*, p^*) \in \mathbf{u}^0 \times Q$ such that

$$a(\mathbf{u}^*, \mathbf{v}^*) - b(\mathbf{v}^*, p^*) = G(g^D, \mathbf{v}^*) \quad \forall \mathbf{v}^* \in \mathbf{u}^0, \quad (3a)$$

$$b(\mathbf{u}^*, r^*) = L(q^*, r^*) \quad \forall r^* \in Q, \quad (3b)$$

where

$$\begin{aligned} a(\mathbf{u}^*, \mathbf{v}^*) &= \sum_{i=1}^2 (\mathbf{K}_i^{-1} \mathbf{u}_i, \mathbf{v}_i)_{\Omega_i} + (\hat{\eta}_\gamma \hat{\mathbf{u}}_\gamma, \hat{\mathbf{v}}_\gamma)_\gamma \\ &\quad + (\eta_\gamma \{\mathbf{u} \cdot \mathbf{n}\}_\gamma, \{\mathbf{v} \cdot \mathbf{n}\}_\gamma)_\gamma + (\zeta_\gamma \eta_\gamma [\![\mathbf{u} \cdot \mathbf{n}]\!]_\gamma, [\![\mathbf{v} \cdot \mathbf{n}]\!]_\gamma)_\gamma, \\ b(\mathbf{u}^*, r^*) &= \sum_{i=1}^2 (\nabla \cdot \mathbf{u}_i, r_i)_{\Omega_i} + (\nabla_\tau \cdot \hat{\mathbf{u}}_\gamma, \hat{r}_\gamma)_\gamma - ([\![\mathbf{u} \cdot \mathbf{n}]\!]_\gamma, \hat{r}_\gamma)_\gamma, \\ G(g^D, \mathbf{v}^*) &= - \sum_{i=1}^2 (g_i^D, \mathbf{v}_i \cdot \mathbf{n}_\Gamma)_{\Gamma_i^D} - (\hat{g}_\gamma^D, \hat{\mathbf{v}}_\gamma \cdot \mathbf{n}_\Gamma)_{\partial\gamma^D}, \\ L(q^*, r^*) &= \sum_{i=1}^2 (q_i, r_i)_{\Omega_i} + (\hat{q}_\gamma, \hat{r}_\gamma)_\gamma. \end{aligned}$$

Using the spaces $\mathbf{u}_h^0 \subset \mathbf{u}^0$ and $Q_h \subset Q$, the discrete approximation of the weak formulation (3) can be written as: find $(\mathbf{u}_h^*, p_h^*) \in \mathbf{u}_h^0 \times Q_h$ such that

$$a(\mathbf{u}_h^*, \mathbf{v}_h^*) - b(\mathbf{v}_h^*, p_h^*) = G(g^D, \mathbf{v}_h^*) \quad \forall \mathbf{v}_h^* = (\mathbf{v}_h^1, \mathbf{v}_h^2, \hat{\mathbf{v}}_\gamma^*) \in \mathbf{u}_h^0, \quad (4a)$$

$$b(\mathbf{u}_h^*, r_h^*) = L(q^*, r_h^*) \quad \forall r_h^* = (r_h^1, r_h^2, \hat{r}_\gamma^*) \in Q_h. \quad (4b)$$

Remark 2.1. Let $\tilde{\mathbf{u}}^0 = \{\mathbf{v}^* \in \mathbf{u}^0 : b(\mathbf{v}^*, r^*) = 0 \ \forall r^* \in Q\}$. The weak formulation (3) admits a unique solution since that the bilinear form $a(\cdot, \cdot)$ is continuous and $\tilde{\mathbf{u}}^0$ -elliptic and the bilinear form $b(\cdot, \cdot)$ is continuous and satisfies the *inf-sup* condition [cf. Martin et al., 2005]. Moreover, the well posedness of the discrete problem (4) holds due to that $a(\cdot, \cdot)$ is discrete $\tilde{\mathbf{u}}^0$ -elliptic and $b(\cdot, \cdot)$ satisfies the discrete *inf-sup* condition [cf. Brezzi and Fortin, 1991].

Remark 2.2. For the problem with intersecting fractures, besides the interface conditions across the fractures mentioned in (2), the reduced model should also be coupled with additional coupling conditions at the intersection points for the fracture-fracture system. The coupling condition at the intersection point has been proposed in Fumagalli [2012] and Formaggia et al. [2014], which together with the reduced model (2) yields the complete reduced model for the problem with intersecting fractures. The associated weak formulation can also be written and solved by the mixed finite element method [cf. Fumagalli, 2012].

3. Adaptive Mixed Finite Element Method

Locally conservative schemes, in particular, the mixed finite element methods, are popular schemes for subsurface fluid flow [see, e.g., Dawson et al., 2004; Ervin et al., 2009; Moortgat et al., 2011; Sun and Wheeler, 2005, 2006, 2007, and references therein]. A reasonable a posteriori error estimator is important for the mesh adaption in the AMFEM. We will test the error indicator derived from the error estimate between the reduced model and its discrete version. The derivation of the a posteriori error estimator can be accomplished by the following several steps:

1. Step 1. Derive the upper bound for $\|\mathbf{u}^* - \mathbf{u}_h^*\|_{\mathbf{u}}$:

$$C \|\mathbf{u}^* - \mathbf{u}_h^*\|_{\mathbf{u}} \leq \sup_{\substack{\mathbf{v}^* \in \tilde{\mathbf{u}}^0 \\ \mathbf{v}^* \neq 0}} \frac{a(\mathbf{u}^* - \mathbf{u}_h^*, \mathbf{v}^*)}{\|\mathbf{v}^*\|_{\mathbf{u}}} + \left(\sum_{i=1}^2 \sum_{T \in \mathcal{T}_h^i} \eta_{T,2}^2 + \sum_{e \in \mathcal{T}_h^\gamma} \eta_{e,\gamma,2}^2 \right)^{\frac{1}{2}}.$$

2. Step 2. Derive the upper bound for $\|p^* - p_h^*\|_Q$:

$$\|p^* - p_h^*\|_Q \leq C \sup_{\substack{\mathbf{v}^* \in \mathbf{u}^0 \\ \mathbf{v}^* \neq 0, \llbracket \mathbf{v} \cdot \mathbf{n} \rrbracket_\gamma = 0}} \frac{b(\mathbf{v}^*, p^* - p_h^*)}{\|\mathbf{v}^*\|_{\mathbf{u}}}.$$

3. Step 3. Derive the upper bound for $a(\mathbf{u}^* - \mathbf{u}_h^*, \mathbf{v}^*)$ and $b(\mathbf{v}^*, p^* - p_h^*)$.

Now we start with some notations. For $i = 1, 2$, we denote by $\mathcal{E}_h(\Omega_i)$ the set of all the edges of the triangulation \mathcal{T}_h^i , $\mathcal{E}_h^0(\Omega_i)$ the set of all the interior edges of the triangulation \mathcal{T}_h^i , $\mathcal{E}_h(\Gamma_i^D)$ the set of all boundary edges on Γ_i^D , and \mathcal{E}_h the set of all edges of the triangulations $\mathcal{T}_h^1 \cup \mathcal{T}_h^2$. We set $\mathcal{T}_h = \mathcal{T}_h^1 \cup \mathcal{T}_h^2$. We denote by $\mathcal{N}_h^0(\gamma)$ the set of interior vertices on \mathcal{T}_h^γ . Let h_T be the diameter of element T for any $T \in \mathcal{T}_h$ and h_e be the diameter of e for any edge $e \in \mathcal{E}_h$. For any interior edge $e = \partial T \cap \partial T'$ in $\mathcal{E}_h^0(\Omega_i)$, $i = 1, 2$, we denote by $[\![\psi]\!]= (\psi|_T)|_e - (\psi|_{T'})|_e$ the jump of scalar function ψ across e . For any edge $e \in \mathcal{E}_h$, we let \mathbf{s}_e be the unit tangential vector along e and \mathbf{n}_e be the unit normal vector along e . We write \mathbf{s} instead of \mathbf{s}_e if no confusion is possible. We denote by \mathcal{P}_e the L^2 -projection operator from $L^2(e)$ onto $\mathbb{P}_k(e)$ for any $e \in \mathcal{E}_h$. In order to derive robust a posteriori error estimator for the discrete problem (4), in the following, we assume $g_i^D \in H^1(e)$ on each $e \in \mathcal{E}_h(\Gamma_i^D)$ and the trace of p_i is $H^{1/2}(e)$ on each $e \in \mathcal{T}_h^i$ for $i = 1, 2$. In the following, we denote by C with or without subscript a positive constant depending only on the shape regularity of the meshes and the polynomial degree. These constants can take on different values in different occurrences.

Given (\mathbf{u}_h^*, p_h^*) the unique solution of the discrete problem (4), we first define for each triangle $T \in \mathcal{T}_h^i$, the a posteriori error estimator

$$\eta_T^2 = \eta_{T,1}^2 + \eta_{T,2}^2 + \eta_{T,3}^2,$$

where $\eta_{T,1}^2 = h_T^2 \|\operatorname{curl}(\mathbf{K}_i^{-1} \mathbf{u}_h^i)\|_{0,T}^2$, $\eta_{T,2}^2 = \|q_i - \nabla \cdot \mathbf{u}_h^i\|_{0,T}^2$, $\eta_{T,3}^2 = h_T^2 \|\mathbf{K}_i^{-1} \mathbf{u}_h^i + \nabla p_h^i\|_{0,T}^2$, $i = 1, 2$, and for each edge e in the interior of Ω_i , the a posteriori error estimator

$$\eta_e^2 = h_e \|\llbracket \mathbf{K}_i^{-1} \mathbf{u}_h^i \cdot \mathbf{s} \rrbracket\|_{0,e}^2, \quad i = 1, 2.$$

Similarly, for $e \in \mathcal{E}_h(\Gamma_i^D)$, $i = 1, 2$, we set

$$\begin{aligned} \eta_{e,\Gamma_i^D}^2 &= h_e \|\mathbf{K}_i^{-1} \mathbf{u}_h^i \cdot \mathbf{s} + \frac{dg_i^D}{ds}\|_{0,e}^2, \\ \operatorname{osc}_{e,\Gamma_i^D}^2 &= h_e \|g_i^D - \mathcal{P}_e g_i^D\|_{0,e}^2. \end{aligned}$$

For each $e \in \mathcal{T}_h^\gamma$, we set

$$\eta_{e,\gamma}^2 = \eta_{e,\gamma,1}^2 + \eta_{e,\gamma,2}^2 + \eta_{e,\gamma,3}^2,$$

where

$$\begin{aligned} \eta_{e,\gamma,1}^2 &= \sum_{i=1}^2 h_e^2 \|(\mathbf{K}_i^{-1} \mathbf{u}_h^i + \nabla p_h^i) \cdot \boldsymbol{\tau}\|_{0,e}^2 + \|\{p_h\}_\gamma - \hat{p}_h^\gamma - \zeta_\gamma \eta_\gamma \llbracket \mathbf{u}_h \cdot \mathbf{n} \rrbracket_\gamma\|_{0,e}^2 \\ &\quad + \|\llbracket p_h \rrbracket_\gamma - \eta_\gamma \{\mathbf{u}_h \cdot \mathbf{n}\}_\gamma\|_{0,e}^2 + \sum_{i=1}^2 \|p_h^i - \Pi_h^i p_h^i\|_{0,e}^2 + \|\hat{p}_h^\gamma - \Pi_h^\gamma \hat{p}_h^\gamma\|_{0,e}^2, \end{aligned}$$

$$\eta_{e,\gamma,2}^2 = \|\hat{q}_\gamma - \nabla_\tau \cdot \hat{\mathbf{u}}_h^\gamma + \llbracket \mathbf{u}_h \cdot \mathbf{n} \rrbracket_\gamma\|_{0,e}^2 \quad \text{and} \quad \eta_{e,\gamma,3}^2 = h_e^2 \|(\hat{\eta}_\gamma \hat{\mathbf{u}}_h^\gamma + \nabla_\tau \hat{p}_h^\gamma) \cdot \boldsymbol{\tau}\|_{0,e}^2.$$

Here $\Pi_h^i : Q_{i,h}|_\gamma \rightarrow C^0(\gamma) \cap (Q_{i,h}|_\gamma)$, $i = 1, 2$ and $\Pi_h^\gamma : Q_{\gamma,h} \rightarrow C^0(\gamma) \cap Q_{\gamma,h}$ are continuous piecewise interpolation operators defined on γ when the polynomial degree $k \geq 1$. When $k = 0$, $\Pi_h^i|_{i=1,2}$ and Π_h^γ are continuous piecewise linear interpolation operators. Let $e_d \in \mathcal{T}_h^\gamma$, $\partial_\gamma^D \in \partial e_d$, and $T_i^* \in \mathcal{T}_h^i$, $e_d \subset \partial T_i^*$ for $i = 1, 2$. For ∂_γ^D , we set

$$\eta_{\partial_\gamma^D}^2 = \sum_{i=1}^2 h_{e_d} (g_i^D - (p_h^i|_{T_i^*})|_{\partial_\gamma^D})^2 + h_{e_d} (\hat{g}_\gamma^D - \hat{p}_h^\gamma|_{\partial_\gamma^D})^2.$$

Then, the global a posteriori error estimator is defined as

$$\eta^2 := \sum_{i=1}^2 \left(\sum_{T \in \mathcal{T}_h^i} \eta_T^2 + \sum_{e \in \mathcal{E}_h^0(\Omega_i)} \eta_e^2 + \sum_{e \in \mathcal{E}_h(\Gamma_i^D)} \eta_{e, \Gamma_i^D}^2 \right) + \sum_{e \in \mathcal{T}_h} \eta_{e, \gamma}^2 + \eta_{\partial \gamma}^2.$$

Actually the error indicator η can be obtained from the derivation of upper bound estimate for the error as follows:

$$\|\mathbf{u}^* - \mathbf{u}_h^*\|_{\mathbf{u}} + \|p^* - p_h^*\|_Q \leq C_{\text{rel}} (\eta + \text{osc}_{\Gamma^D}),$$

$$\text{where } \text{osc}_{\Gamma^D} = \left(\sum_{i=1}^2 \sum_{e \in \mathcal{E}_h(\Gamma_i^D)} \text{osc}_{e, \Gamma_i^D}^2 \right)^{1/2}.$$

4. Effective Permeability

Since the permeability in the fracture is usually quite different from that in the matrix block, the fractured porous media can be viewed as porous media with heterogeneous permeability. The objective of this section is to compute the effective permeability of the whole fractured porous media which can reveal how the fractures of certain assignment can affect the anisotropic flow in a larger scale. For simplicity, we assume Ω is a two-dimensional rectangular domain (see Figure 2). Flow-based upscaling of permeability has become an important approach to simulate the fluid flow in heterogeneous porous media. To obtain the effective permeability, we study the scale-up of single-phase flow through the fractured porous media. Following Wu *et al.* [2002] and Wen and Gomez-Hernandez [1996], the effective permeability tensor \mathbf{K}_{eff} of the porous media can be defined as:

$$\mathbf{K}_{\text{eff}} \langle \nabla p \rangle_{\Omega} := -\langle \mathbf{u} \rangle_{\Omega}, \quad (5)$$

where p and \mathbf{u} are solutions of (1) in Ω with appropriate boundary conditions, and

$$\langle \cdot \rangle_{\Omega} = \frac{1}{|\Omega|} \int_{\Omega} (\cdot) d\mathbf{x}.$$

is the volume average over Ω . To determine \mathbf{K}_{eff} in (5), we need two sets of fine-scale flow solutions in Ω , \mathbf{u}_k , and p_k , $k = 1, 2$, which can be obtained from

$$\mathbf{u}^k = -\mathbf{K} \nabla p^k \text{ and } \nabla \cdot \mathbf{u}^k = 0 \quad \text{in } \Omega.$$

The above equation is well posed with appropriate boundary conditions. Define $w^k = p^k - x_k$, $k = 1, 2$. The main challenge of the flow-based upscaling method is how to impose local boundary conditions. We will use the open-side boundary condition and the sealed-side boundary condition as:

$$w^k = 0 \quad \text{on } \partial\Omega; \quad (6)$$

$$w^k = 0 \text{ on } \Gamma_k, \quad \mathbf{u}^k \cdot \mathbf{n} = 0 \text{ on } \Gamma_l, \quad k, l = 1, 2, \quad k \neq l, \quad (7)$$

where Γ_k is the parts of $\partial\Omega$ normal to unit vector \mathbf{e}_k . There are other choices of boundary conditions, here we only consider the above two types of boundary conditions since they are simple and easy to implement in practice. We mention that the oversampling technique may also be used to reduce the influence of setting of boundary conditions.

We assume that there is a single fracture in Ω which can be nonimmersed, partially immersed, or totally immersed in the porous media (see Figure 2). The analysis in the sequel can be immediately extended to the problem with more reduced nonintersecting fractures. Since we utilize the reduced model (2), the computations of $\langle \nabla p^k \rangle_{\Omega}$ and $\langle \mathbf{u}^k \rangle_{\Omega}$ will be based on (2) and the corresponding boundary conditions.

We first consider the details about the flow-based upscaling method using open-side boundary condition (6) to derive the effective permeability tensor. For simplicity, we consider the case with the reduced fracture γ nonimmersed in Ω . The other two cases in Figure 2 can be similarly analyzed. Then, Ω is separated into two subdomains Ω_1 and Ω_2 connected by γ . Let $p^k = (p_1^k, p_2^k, \hat{p}_{\gamma}^k)$ and $\mathbf{u}^k = (\mathbf{u}_1^k, \mathbf{u}_2^k, \hat{\mathbf{u}}_{\gamma}^k, \hat{\mathbf{u}}_{\mathbf{n}}^{\gamma, k})$. Here p_i^k and \mathbf{u}_i^k denote the pressure and velocity in Ω_i , and $\hat{p}_{\gamma}^k, \hat{\mathbf{u}}_{\gamma}^k, \hat{\mathbf{u}}_{\mathbf{n}}^{\gamma, k}$ denote the pressure, the tangential component, and normal component of velocity along γ . In such a case, if (6) holds, $\langle \nabla p^k \rangle_{\Omega}$ is computed as:

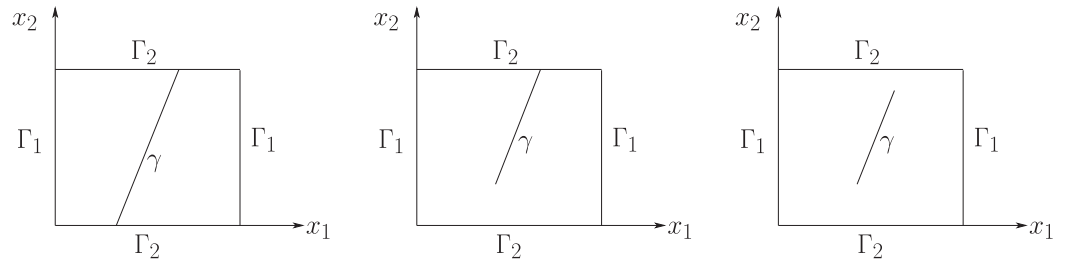


Figure 2. The domain Ω with the reduced fracture (left) nonimmersed, (middle) partially immersed, and (right) totally immersed in Ω .

$$\langle \nabla p^k \rangle_{\Omega} = \mathbf{e}_k + \frac{1}{|\Omega|} \int_{\partial\Omega} w^k \mathbf{n}_{\Gamma} ds = \mathbf{e}_k. \quad (8)$$

However, the flow in the fractured porous media is simulated by the reduced model (2), then we compute $\langle \mathbf{u}^k \rangle_{\Omega}$ as follows:

$$\langle \mathbf{u}^k \rangle_{\Omega} = \frac{1}{|\Omega|} \left(\int_{\Omega_1} \mathbf{u}_1^k d\mathbf{x} + \int_{\Omega_2} \mathbf{u}_2^k d\mathbf{x} + \int_{\gamma} (\hat{\mathbf{u}}_{\gamma}^k + \hat{\mathbf{u}}_{\mathbf{n}}^{\gamma,k}) ds \right), \quad (9)$$

where $\hat{\mathbf{u}}_{\mathbf{n}}^{\gamma,k} = d(s) \{ \mathbf{u}^k \cdot \mathbf{n} \}_{\gamma} \mathbf{n}$ simulates the normal component of Darcy velocity along γ . Combining (8) and (9), we have

$$\mathbf{e}_l \cdot (\mathbf{K}_{\text{eff}} \mathbf{e}_k) = - \frac{1}{|\Omega|} \left(\int_{\Omega_1} \mathbf{u}_1^k d\mathbf{x} + \int_{\Omega_2} \mathbf{u}_2^k d\mathbf{x} + \int_{\gamma} (\hat{\mathbf{u}}_{\gamma}^k + \hat{\mathbf{u}}_{\mathbf{n}}^{\gamma,k}) ds \right) \cdot \mathbf{e}_l.$$

Noting that

$$\left(\sum_{i=1}^2 \int_{\Omega_i} \mathbf{u}_i^k d\mathbf{x} \right) \cdot \mathbf{e}_l = \left(\sum_{i=1}^2 \int_{\Omega_i} \mathbf{u}_i^k d\mathbf{x} \right) \cdot (\nabla p^l - \nabla w^l)$$

and

$$\int_{\Omega_i} \mathbf{u}_i^k \cdot \nabla w^l d\mathbf{x} = \int_{\partial\Omega_i} \mathbf{u}_i^k \cdot \mathbf{n}_i w^l ds, \quad i=1, 2,$$

where \mathbf{n}_i is the unit outward normal to Ω_i , we have

$$\begin{aligned} - \left(\sum_{i=1}^2 \int_{\Omega_i} \mathbf{u}_i^k d\mathbf{x} \right) \cdot \mathbf{e}_l &= \sum_{i=1}^2 \int_{\Omega_i} \mathbf{K}_i \nabla p_i^k \cdot \nabla p^l d\mathbf{x} \\ &+ \int_{\gamma} \{ \mathbf{u}^k \cdot \mathbf{n} \}_{\gamma} \{ w^l \}_{\gamma} ds + \int_{\gamma} \{ \mathbf{u}^k \cdot \mathbf{n} \}_{\gamma} \{ [w^l] \}_{\gamma} ds. \end{aligned} \quad (10)$$

Let $\mathbf{e}_l = \mathbf{e}_l^{\tau} + \mathbf{e}_l^{\mathbf{n}}$, where $\mathbf{e}_l^{\tau} = (\mathbf{e}_l \cdot \boldsymbol{\tau}) \boldsymbol{\tau}$ and $\mathbf{e}_l^{\mathbf{n}} = (\mathbf{e}_l \cdot \mathbf{n}) \mathbf{n}$. Then,

$$\int_{\gamma} (\hat{\mathbf{u}}_{\gamma}^k + \hat{\mathbf{u}}_{\mathbf{n}}^{\gamma,k}) ds \cdot \mathbf{e}_l = \int_{\gamma} \hat{\mathbf{u}}_{\gamma}^k ds \cdot \mathbf{e}_l^{\tau} + \int_{\gamma} \hat{\mathbf{u}}_{\mathbf{n}}^{\gamma,k} ds \cdot \mathbf{e}_l^{\mathbf{n}}.$$

Let $\hat{\mathbf{u}}_{\gamma}^k = \hat{p}_{\gamma}^k - x_k$, $k=1, 2$. By the reduced equation ((2a)d), we get

$$\int_{\gamma} \hat{\mathbf{u}}_{\gamma}^k ds \cdot \mathbf{e}_l^{\tau} = \int_{\gamma} \hat{\mathbf{u}}_{\gamma}^k \cdot (\nabla_{\tau} \hat{p}_{\gamma}^l - \nabla_{\tau} \hat{w}_{\gamma}^l) ds = - \int_{\gamma} \hat{\eta}_{\gamma}^{-1} \nabla_{\tau} \hat{p}_{\gamma}^k \cdot \nabla_{\tau} \hat{p}_{\gamma}^l ds - \int_{\gamma} \hat{\mathbf{u}}_{\gamma}^k \cdot \nabla_{\tau} \hat{w}_{\gamma}^l ds.$$

By integration by parts, (6) and (2c),

$$- \int_{\gamma} \hat{\mathbf{u}}_{\gamma}^k \cdot \nabla_{\tau} \hat{w}_{\gamma}^l ds = \int_{\gamma} \nabla_{\tau} \cdot \hat{\mathbf{u}}_{\gamma}^k \hat{w}_{\gamma}^l ds = \int_{\gamma} \{ \mathbf{u}^k \cdot \mathbf{n} \}_{\gamma} \hat{w}_{\gamma}^l ds.$$

Therefore,

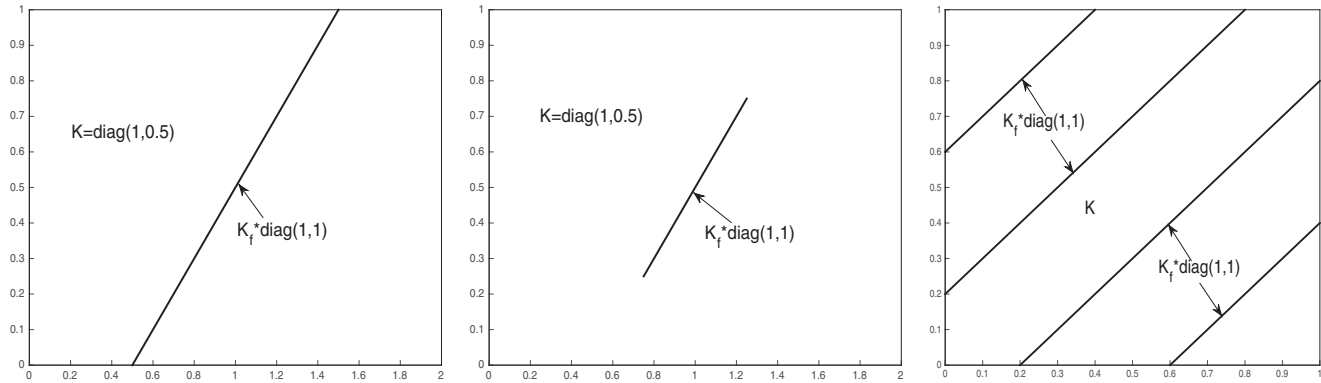


Figure 3. The matrix block and reduced fracture for the (left) first case and (middle) second case of Example 5.1. The matrix block and reduced fractures for the (right) third and fourth cases of Example 5.1.

$$\int_{\gamma} \hat{\mathbf{u}}_{\gamma}^k ds \cdot \mathbf{e}_f^r = - \int_{\gamma} \hat{\eta}_{\gamma}^{-1} \nabla_{\tau} \hat{p}_{\gamma}^k \cdot \nabla_{\tau} \hat{p}_{\gamma}^l ds + \int_{\gamma} [\![\mathbf{u}^k \cdot \mathbf{n}]\!] \hat{w}_{\gamma}^l ds. \quad (11)$$

Moreover, by the definition of $\hat{\mathbf{u}}_n^{\gamma,k}$ and the interface condition (2f), we have

$$\int_{\gamma} \hat{\mathbf{u}}_n^{\gamma,k} ds \cdot \mathbf{e}_f^n = \int_{\gamma} d(s) \{ \mathbf{u}^k \cdot \mathbf{n} \}_{\gamma} (\mathbf{e}_f \cdot \mathbf{n}) ds = \int_{\gamma} \mathbf{K}_{f,n} [\![p^k]\!]_{\gamma} (\mathbf{e}_f \cdot \mathbf{n}) ds. \quad (12)$$

By the above equalities (10)–(12), the interface condition (2e) and the definitions of w^k and \hat{w}_{γ}^k , we obtain

$$\begin{aligned} \mathbf{e}_f \cdot (\mathbf{K}_{\text{eff}} \mathbf{e}_k) |\Omega| &= \sum_{l=1}^2 \int_{\Omega_l} \mathbf{K}_l \nabla p_l^k \cdot \nabla p_l^l d\mathbf{x} + \int_{\gamma} \hat{\eta}_{\gamma}^{-1} \nabla_{\tau} \hat{p}_{\gamma}^k \cdot \nabla_{\tau} \hat{p}_{\gamma}^l ds \\ &+ \int_{\gamma} \xi_{\gamma} \eta_{\gamma} [\![\mathbf{u}^k \cdot \mathbf{n}]\!]_{\gamma} [\![\mathbf{u}^l \cdot \mathbf{n}]\!]_{\gamma} ds + \int_{\gamma} \eta_{\gamma} \{ \mathbf{u}^k \cdot \mathbf{n} \}_{\gamma} \{ \mathbf{u}^l \cdot \mathbf{n} \}_{\gamma} ds - \int_{\gamma} \mathbf{K}_{f,n} [\![p^k]\!]_{\gamma} (\mathbf{e}_f \cdot \mathbf{n}) ds. \end{aligned}$$

When the fracture behaves as conductor or barrier in the porous media, the absolute value of $\int_{\gamma} \hat{\mathbf{u}}_n^{\gamma,k} ds \cdot \mathbf{e}_f^n$ is actually small. This will also be clarified in the numerical experiments. Then, we can compute $\mathbf{K}_{\text{eff}}^* \approx \mathbf{K}_{\text{eff}}^*$ as follows:

$$\begin{aligned} \mathbf{e}_f \cdot (\mathbf{K}_{\text{eff}}^* \mathbf{e}_k) |\Omega| &= \sum_{l=1}^2 \int_{\Omega_l} \mathbf{K}_l \nabla p_l^k \cdot \nabla p_l^l d\mathbf{x} + \int_{\gamma} \hat{\eta}_{\gamma}^{-1} \nabla_{\tau} \hat{p}_{\gamma}^k \cdot \nabla_{\tau} \hat{p}_{\gamma}^l ds \\ &+ \int_{\gamma} \xi_{\gamma} \eta_{\gamma} [\![\mathbf{u}^k \cdot \mathbf{n}]\!]_{\gamma} [\![\mathbf{u}^l \cdot \mathbf{n}]\!]_{\gamma} ds + \int_{\gamma} \eta_{\gamma} \{ \mathbf{u}^k \cdot \mathbf{n} \}_{\gamma} \{ \mathbf{u}^l \cdot \mathbf{n} \}_{\gamma} ds. \end{aligned}$$

Hence, $\mathbf{K}_{\text{eff}}^*$ is symmetric and positive definite. Let λ_{\max} and λ_{\min} be the maximum and minimum eigenvalues of \mathbf{K}_{eff} , and λ_{\max}^* and λ_{\min}^* be the maximum and minimum eigenvalues of $\mathbf{K}_{\text{eff}}^*$. We define two parameters

$$\alpha = \lambda_{\max} / \lambda_{\min} \quad \text{and} \quad \alpha^* = \lambda_{\max}^* / \lambda_{\min}^*.$$

Since $\mathbf{K}_{\text{eff}}^*$ is symmetric and positive definite, we denote β^* by the angle of principal direction of $\mathbf{K}_{\text{eff}}^*$. Define a rotation matrix \mathbf{R}_{β^*} as:

$$\mathbf{R}_{\beta^*} = \begin{pmatrix} \cos \beta^* & \sin \beta^* \\ -\sin \beta^* & \cos \beta^* \end{pmatrix}.$$

Then, it holds that $\mathbf{K}_{\text{eff}}^* = \mathbf{R}_{\beta^*}^T \hat{\mathbf{K}}_{\text{eff}} \mathbf{R}_{\beta^*}$, where $\hat{\mathbf{K}}_{\text{eff}} = \text{diag}(\lambda_{\max}^*, \lambda_{\min}^*)$. The influence of the fractures on the parameters α , α^* , and β^* will be observed in the numerical experiments.

For the flow-based upscaling method using sealed-side boundary condition (7), $\langle \mathbf{u}^k \rangle_{\Omega}$ is computed as (9). However, $\langle \nabla p^k \rangle_{\Omega}$ is computed as:

Table 1. The First Case of Example 5.1^a

$K_f = 10^{-4}$	\mathbf{K}_{eff}	0.6758	0.1621	0.1621	0.4190	α	2.2143	β^*	0.4505
	$\mathbf{K}_{\text{eff}}^*$	0.6758	0.1621	0.1621	0.4190	α^*	2.2145		
$K_f = 10^{-2}$	\mathbf{K}_{eff}	0.8397	0.07941	0.08022	0.4604	α	1.9263	β^*	0.2023
	$\mathbf{K}_{\text{eff}}^*$	0.8381	0.08103	0.08103	0.4596	α^*	1.9295		
$K_f = 10^2$	\mathbf{K}_{eff}	1.3571	0.3500	0.3518	0.8553	α	2.2785	β^*	0.4777
	$\mathbf{K}_{\text{eff}}^*$	1.3535	0.3536	0.3536	0.8535	α^*	2.2916		
$K_f = 10^4$	\mathbf{K}_{eff}	36.3589	35.3518	35.3536	35.8571	α	94.7254	β^*	0.7819
	$\mathbf{K}_{\text{eff}}^*$	36.3553	35.3553	35.3553	35.8553	α^*	95.3946		

^aEffective permeability tensor based on the flow-based upscaling method using open-side boundary condition for the first case with single nonimmersed fracture.

$$\langle \nabla p^k \rangle_{\Omega} = \frac{1}{|\Omega|} \left(\sum_{i=1}^2 \int_{\partial \Omega_i \setminus \gamma} p_i^k \mathbf{n}_i ds + \sum_{z \in \partial \gamma \cap \partial \Omega} d_z (\hat{p}_z^k \mathbf{n}_{\Gamma})|_z \right), \quad (13)$$

where d_z is the thickness of fracture at z . Then, in such a case, the effective permeability tensor \mathbf{K}_{eff} is non-symmetric. Since the thickness of fracture is usually small, the second term in the right-hand side of (13) is a small term and can be omitted in the computation.

5. Numerical Experiments

In the following experiments, we choose the parameter ξ (see the definition of ξ_{γ} in section 2.1) in the reduced model (2) as $\xi = 0.75$ and assume that the thickness of fracture is always 0.01 in the experiments if there is no confusion. The source term in (2) is set to be zero in the following examples.

Example 5.1. In this example, we test how the fractures of certain assignment can affect the anisotropic flow in a larger scale by computing the effective permeability of the whole fractured porous media. We choose $k = 1$ both in \mathbf{u}_h^0 and Q_h in this experiment.

First, we consider the reduced model (2) in the domain $\Omega = [0, 2] \times [0, 1]$ with a reduced fracture on the line $L = \{(x, y) : y = x - 0.5, x \in [0.5, 1.5]\}$ which is nonimmersed in Ω (see the left graph of Figure 3). The permeability tensors in the matrix block and the fracture are given by $\mathbf{K} = \text{diag}(1, 0.5)$ and $\mathbf{K}_f = K_f \text{diag}(1, 1)$. Second, we consider the reduced model (2) in the domain $\Omega = [0, 2] \times [0, 1]$ with a reduced fracture on the line $L = \{(x, y) : y = x - 0.5, x \in [0.75, 1.25]\}$ which is immersed in Ω (see the middle graph of Figure 3). The permeability tensors in the matrix block and the fracture are the same as the first case. We employ the flow-based upscaling method using open-side boundary condition to test the effective permeability tensor for the two cases. For the first case, we apply the mixed finite element method (FEM) on quasi-uniform meshes. However, for the second case, the singularity of solution always exists at the ends of the reduced fracture. Thus, we use the AMFEM for the simulation of the second case.

In Tables 1 and 2, the four components of effective permeability tensor are listed in vectorized version, i.e., $\text{vec}(\mathbf{K}_{\text{eff}}) = [K_{\text{eff}}^{11}, K_{\text{eff}}^{21}, K_{\text{eff}}^{12}, K_{\text{eff}}^{22}]$. For the approximation of $\mathbf{K}_{\text{eff}}^*$, the symmetry property of $\mathbf{K}_{\text{eff}}^*$ depends on the round off error in numerical computation. The three parameters α , α^* , and β^* are also reported in the two tables. For the first case with nonimmersed fracture, from Table 1, we can see that the three parameters α , α^* , and β^* increase when K_f tends to be larger or smaller, which indicates the effect of fracture in the porous media. For the second case with immersed fracture, one can observe from Table 2 that the influence of fracture is smaller.

Table 2. The Second Case of Example 5.1^a

$K_f = 10^{-4}$	\mathbf{K}_{eff}	0.8775	0.06126	0.06126	0.4694	α	1.9256	β^*	0.1459
	$\mathbf{K}_{\text{eff}}^*$	0.8775	0.06127	0.06127	0.4694	α^*	1.9256		
$K_f = 10^{-2}$	\mathbf{K}_{eff}	0.9301	0.03463	0.03498	0.4827	α	1.9432	β^*	0.07839
	$\mathbf{K}_{\text{eff}}^*$	0.9294	0.03533	0.03533	0.4824	α^*	1.9437		
$K_f = 10^2$	\mathbf{K}_{eff}	1.05591	0.05220	0.05328	0.5548	α	1.9321	β^*	0.1065
	$\mathbf{K}_{\text{eff}}^*$	1.05404	0.05406	0.05406	0.5540	α^*	1.9330		
$K_f = 10^4$	\mathbf{K}_{eff}	1.09601	0.06433	0.09335	0.5670	α	1.9917	β^*	0.1552
	$\mathbf{K}_{\text{eff}}^*$	1.08017	0.08017	0.08017	0.5802	α^*	1.9250		

^aEffective permeability tensor based on the flow-based upscaling method using open-side boundary condition for the second case with single immersed fracture.

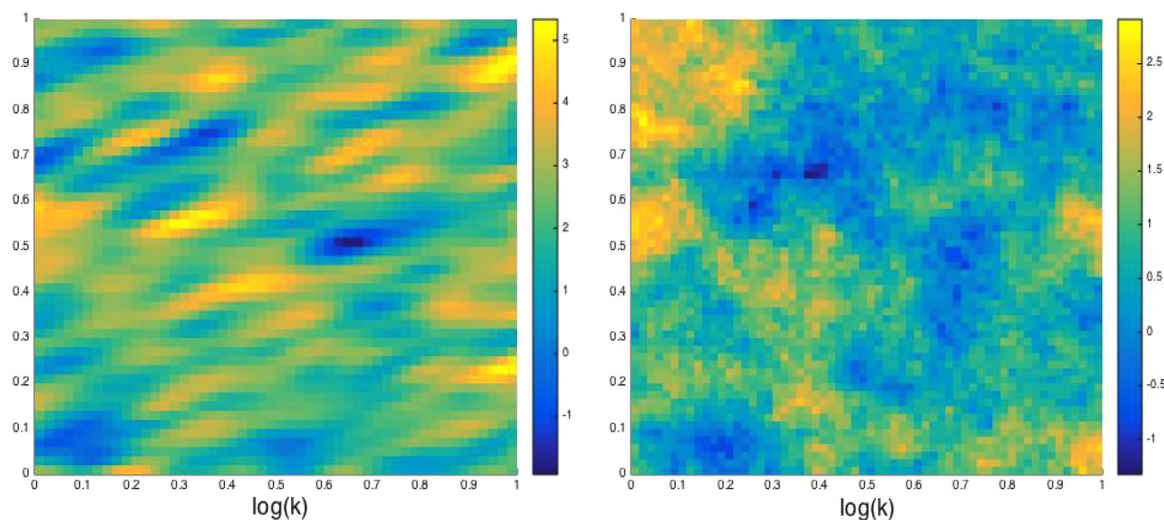


Figure 4. Logarithm distribution of permeability. (left) The 50×50 random field based on Gaussian covariance with rotation angle $\theta = \pi/6$. (right) 60×60 field based on the cutting data from SPE10 data set for the horizontal permeability.

We consider the third and fourth cases for the reduced model (2) in the domain $\Omega = [0, 1] \times [0, 1]$ with four reduced fractures on the lines $L_2 = \{(x, y) : y = x + 0.2, x \in [0, 0.8]\}$, $L_4 = \{(x, y) : y = x - 0.6, x \in [0.6, 1]\}$ which are all nonimmersed in Ω (see the right graph of Figure 3). The permeability tensors in the matrix blocks and the fractures for the third and fourth cases are shown in the right graph of Figure 3. For the third case, the permeability tensor in the matrix blocks is given by $\mathbf{K} = \text{diag}(2\kappa, \kappa)$ where κ is a realization of a 50×50 random field based on Gaussian covariance (cf. Figure 4 and Zhang [2002]). For the fourth case, the permeability tensor in the matrix blocks is given by $\mathbf{K} = \text{diag}(\kappa, \kappa)$ where κ is the horizontal permeability from the SPE10 data set which is obtained from the SPE website (<http://www.spe.org/web/csp/>). We use the 60×60 cutting data of the horizontal permeability in one of the horizontal levels. We test the flow-based upscaling method using the open-side boundary condition and the sealed-side boundary condition based on the mixed FEM on quasi-uniform meshes. The parameters α , α^* , and β^* are reported in Figures 5 and 6. We can observe that the parameters α and α^* are almost the same when the open-side boundary condition is applied. The parameter α based on the open-side boundary condition is always larger than that based on the sealed-side boundary condition for high fracture permeability. This is caused by the fact that in such a case the effective permeability obtained by the open-side boundary condition is always larger than that by the sealed-side boundary condition. The right graphs in Figures 5 and 6 show the variation of the principal direction of \mathbf{K}_{eff} with the permeability in fractures which indicates the effects of fractures on the effective permeability.

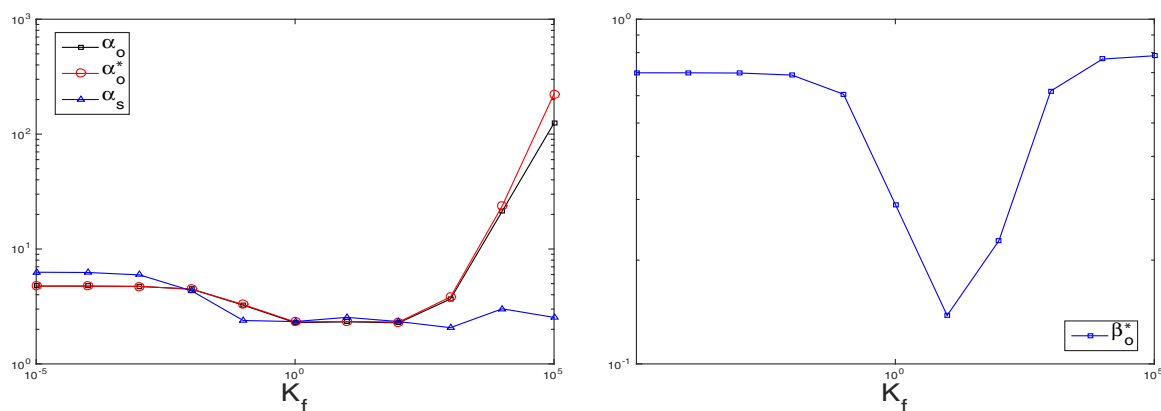


Figure 5. The third case of Example 5.1. (left) α_o and α_o^* by using the open-side boundary condition and α_s using the sealed-side boundary condition. (right) β_o^* by using the open-side boundary condition.

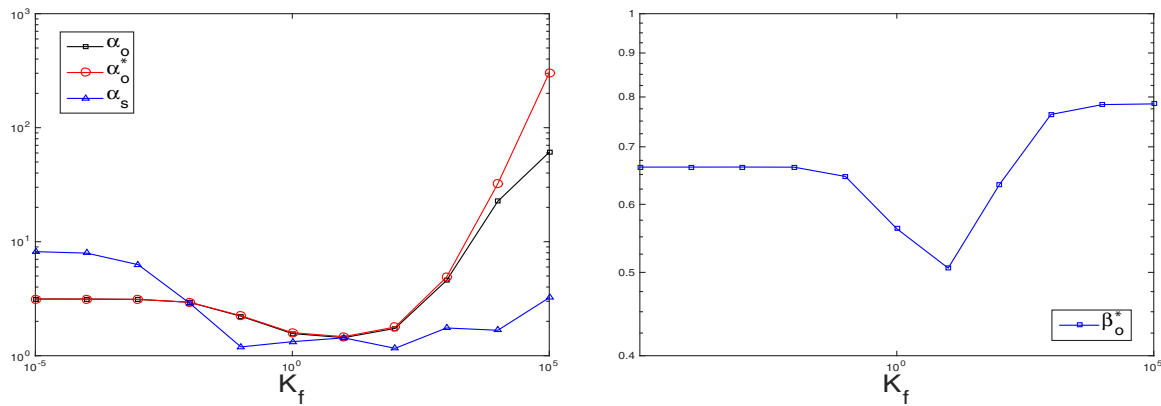


Figure 6. The fourth case of Example 5.1. (left) α_o and α_o^* by using the open-side boundary condition and α_s using the sealed-side boundary condition. (right) β_o^* by using the open-side boundary condition.

Example 5.2. In this example, we first consider a case with three nonintersecting fractures as shown in the left graph of Figure 7. For each fracture, one end point of the fracture is on the inflow boundary and the other end point is in the interior of the domain. Then, we will consider the cases with only one fracture which connects the inflow boundary and the outflow boundary, where the globally imposed pressure gradient tends to drive the fluid in a single direction, but in a local area the fluid can flow backward because of the fractures with large permeability. We choose two types of the pair of finite element spaces $\mathbf{u}_h^0 \times Q_h$ with $k = 1$ and $k = 0$ which are denoted by RT_1P_1 and RT_0P_0 .

For the first case, we consider the reduced model (2) in the domain $\Omega = [0, 2] \times [0, 2]$ with a reduced fracture shown in the left graph of Figure 7. The permeability tensors in the matrix block and the three fractures are given by $\mathbf{K} = K \text{diag}(1, 1)$ and $\mathbf{K}_f = K_f \text{diag}(1, 1)$ where $K = 1$. For the surrounding matrix block, the Dirichlet boundary condition is given by $p = 1$ on $\{0\} \times [0, 2]$ and $p = 0$ on $\{2\} \times [0, 2]$, and homogeneous Neumann boundary condition is imposed on the other part of $\partial\Omega$. Dirichlet boundary conditions hold on the fractures boundaries as $\hat{p}_\gamma = 1$ at the end points $(0, 0.4)$, $(0, 1)$ and $(0, 1.6)$, and homogeneous Neumann boundary conditions are imposed at all the three interior end points. We use the adaptive mixed RT_1P_1 approximation for this case. We first test the case with $K_f = 10^3$. From the left graph of Figure 8, we can observe that the singularity of solution always occurs at the corners and the interior end points of fractures where the local refinement is imposed. The right graph of Figure 8 and the left graph of Figure 9 show the approximate velocity \mathbf{u}_h^* and approximate pressure p_h^* respectively. In this scenario, it is interesting to see that the flow in the two horizontal branches of the top and bottom fractures are toward the right boundary, which probably counters intuition that would suggest the flow in the smaller branches to be toward the left-hand side boundary. This can be explained in light of pressure distribution over the domain, which shows that the pressure along the central fracture is higher than in the neighboring region and this results in the shorter branches of the top and bottom fractures to collect fluid toward the right-hand side boundary. This can

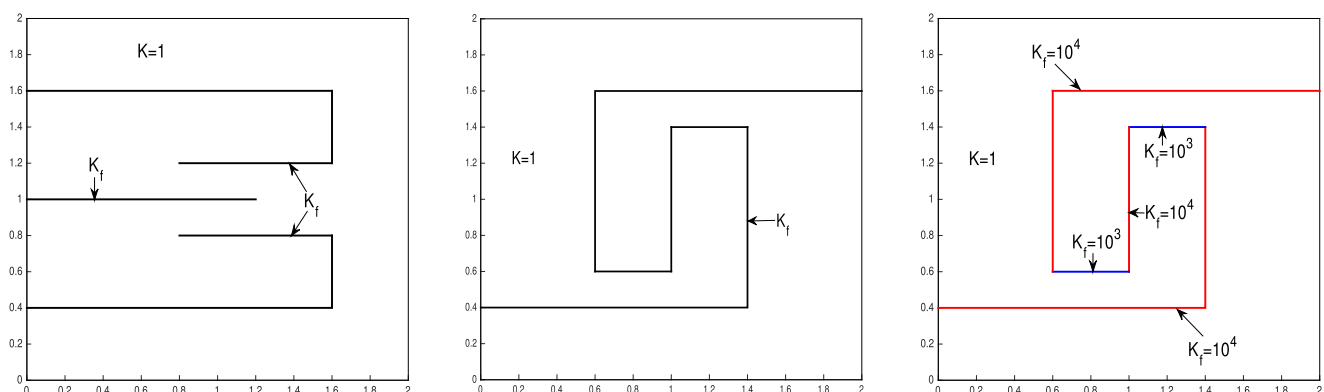


Figure 7. The matrix block and reduced fracture for (left) the first case, (middle) the second case, and (right) the third case of Example 5.2.

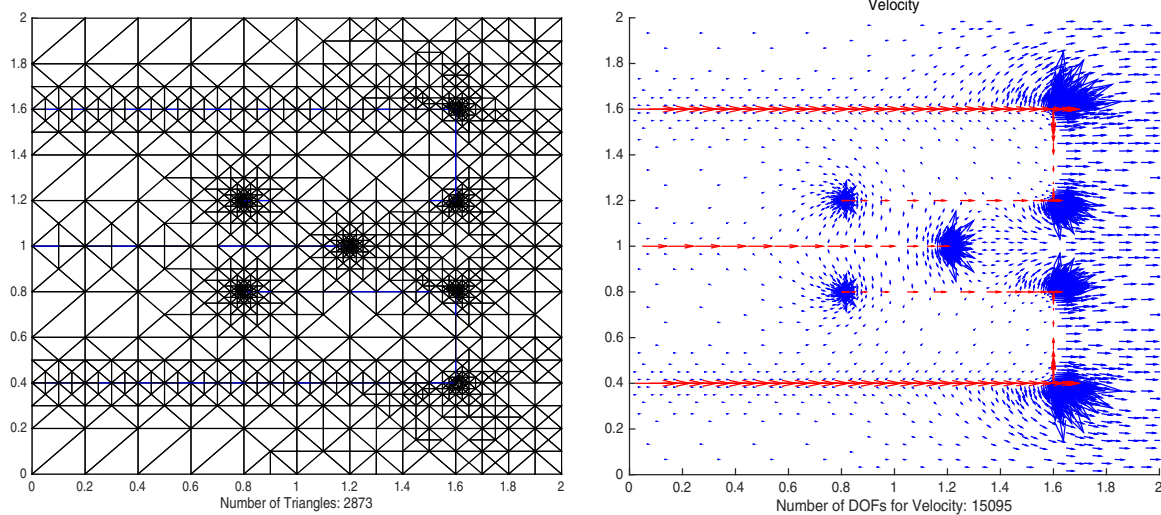


Figure 8. The first case of Example 5.2 with $K_f = 10^3$. Adaptively refined mesh by (left) adaptive mixed RT_1P_1 approximation and (right) the associated approximate velocity \mathbf{u}_h^* .

also be observed from the right graph of Figure 9 for the pressure profiles in matrix block along the line $x = 1$ for the cases with different permeability in fractures. Since the discrete solution of pressure in matrix block is piecewise linear and may be discontinuous, we get the above pressure profiles by interpolation technique. Actually, for this problem, even the permeability in the fractures becomes larger, the fluid in matrix block always flows in a single direction toward the outflow boundary.

Next, we consider the second case for the reduced model (2) in the domain $\Omega = [0, 2] \times [0, 2]$ with a reduced fracture shown in the middle graph of Figure 7. The permeability tensors in the matrix block and the fracture are given by $\mathbf{K} = K \text{diag}(1, 1)$ and $\mathbf{K}_f = K_f \text{diag}(1, 1)$ where $K = 1$ and $K_f = 10^3$. For the surrounding matrix block, the boundary conditions are given as in the first case. Dirichlet boundary conditions hold on the fracture boundaries as $\hat{p}_\gamma = 1$ at the end point $(0, 0.4)$ and $\hat{p}_\gamma = 0$ at another end point $(2, 1.6)$. The AMFEM is tested by RT_1P_1 and RT_0P_0 approximations for this case. Figure 10 displays the adaptively refined mesh, the associated approximate velocity \mathbf{u}_h^* by the adaptive mixed RT_1P_1 approximation and the approximate pressure p_h^* by the adaptive mixed RT_1P_1 approximation. We can see that the a posteriori error estimator η can capture the singularity of solution at the corners of fracture. From the middle graph of Figure 10, we can observe that the globally imposed pressure gradient tends to drive the fluid to the eastern direction, but due to the appearance of fracture with large permeability in the porous media, the fluid can flow backward

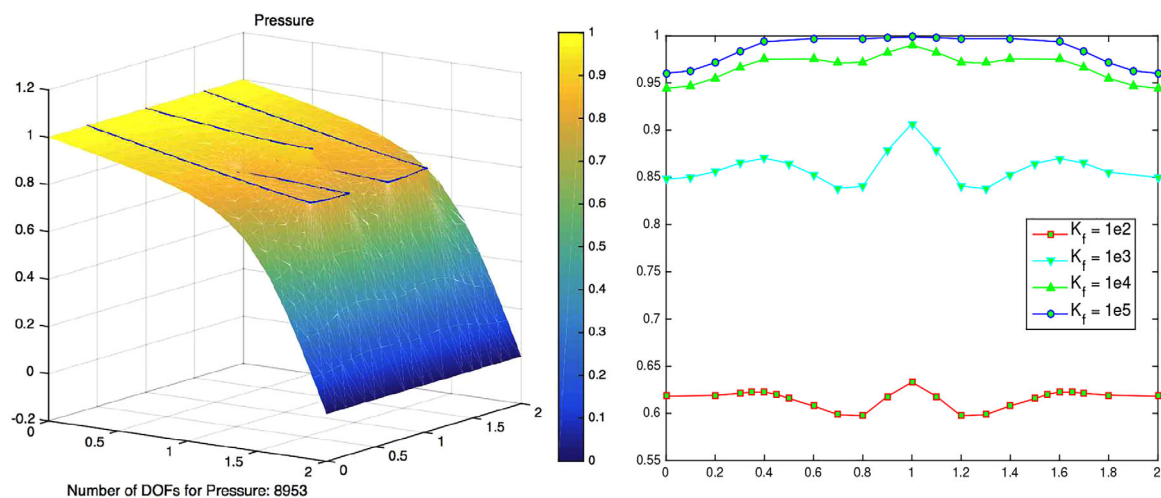


Figure 9. The first case of Example 5.2. (left) The 3-D plot of approximate pressure p_h^* for the case with $K_f = 10^3$. (right) Pressure profiles in matrix block along the line $x = 1$ for the cases with $K_f = 10^2, 10^3, 10^4, 10^5$.

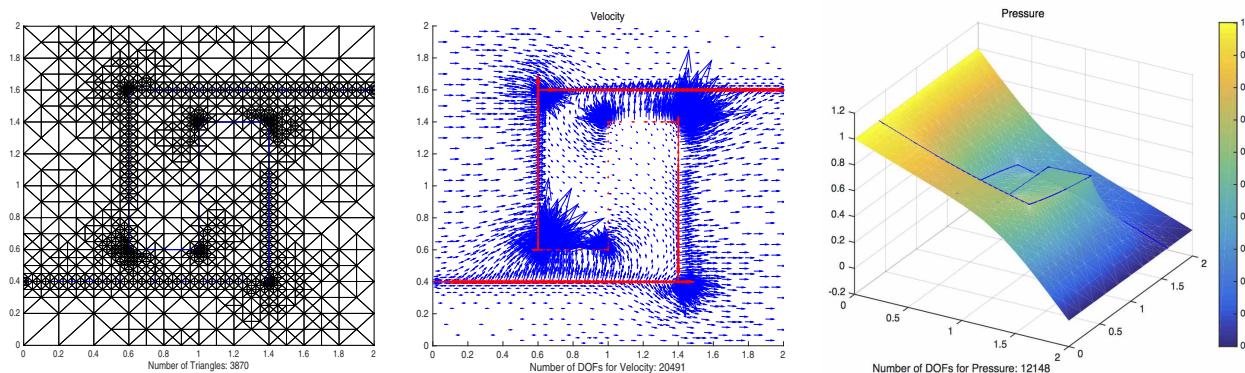


Figure 10. The second case of Example 5.2. (left) Adaptively refined mesh by adaptive mixed RT_1P_1 approximation. (middle) The associated approximate velocity u_h^* . (right) The 3-D plot of approximate pressure p_h^* .

to the western direction in the local area $[0.6, 1.4] \times [0.6, 1.4]$ near the center of domain. The convergence history of the a posteriori error estimator η is displayed in the left graph of Figure 11 based on the adaptive mixed RT_1P_1 and RT_0P_0 approximations on a series of adaptive meshes and the uniform meshes. We can see that the convergence of η based on RT_1P_1 approximation is faster than that based on RT_0P_0 approximation, and the convergence of η on adaptive meshes is also faster than that on the corresponding uniform meshes when using the same pair of finite element spaces. For instance, the number of total degrees of freedom (DOFs) needed to obtain $\eta \approx 0.09$ is 22,035 based on the adaptive mixed RT_1P_1 approximation, however, the total DOFs based on the adaptive mixed RT_0P_0 approximation would be 116,582 to get the similar accuracy.

This scenario is quite interesting, it shows that, for this particular configuration of the fracture orientation, the flow in the part of the fracture which is in the opposite direction to the general direction of the flow creates a domain in the matrix block where the flow is generally opposing the general flow direction and that the intensity of flow reversal is dependent on the permeability of the fracture. This is also manifested by looking at the pressure field distribution over the domain (see the right graph of Figure 10). For instance, the right graph of Figure 11 displays the pressure profiles in matrix block along the line $y = 1$ for the cases with $K_f = 10^2, 500, 10^3, 10^4, 10^5$. It shows that when the permeability in the fracture is not large enough, the phenomenon that the fluid flows backward in a local area will not appear due to the pressure field distribution.

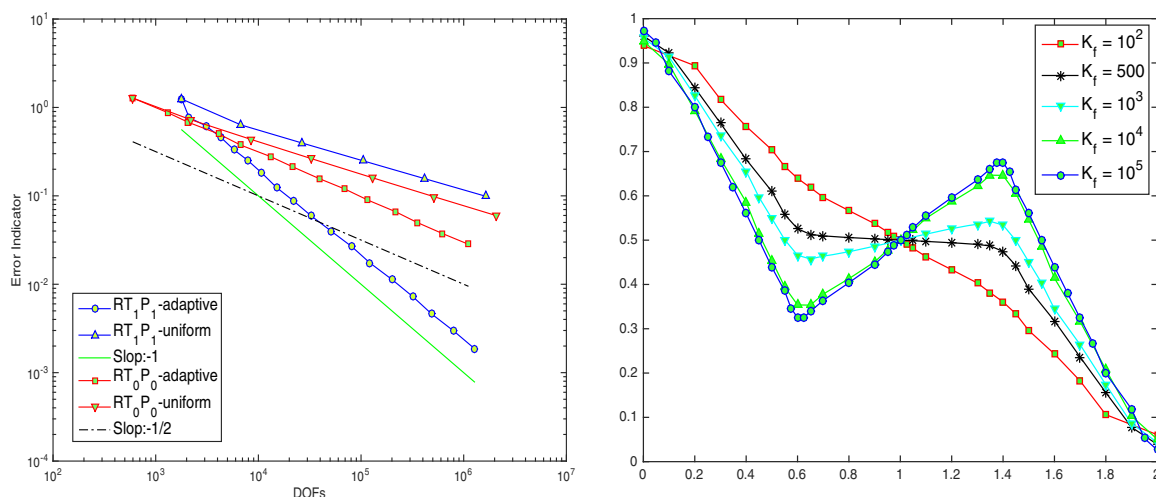


Figure 11. The second case of Example 5.2. (left) Convergence history of η (right) based on the adaptive mixed RT_1P_1 and RT_0P_0 approximations on the adaptive meshes and the uniform meshes. (right) Pressure profiles in matrix block along the line $y = 1$ for the cases with $K_f = 10^2, 500, 10^3, 10^4, 10^5$.

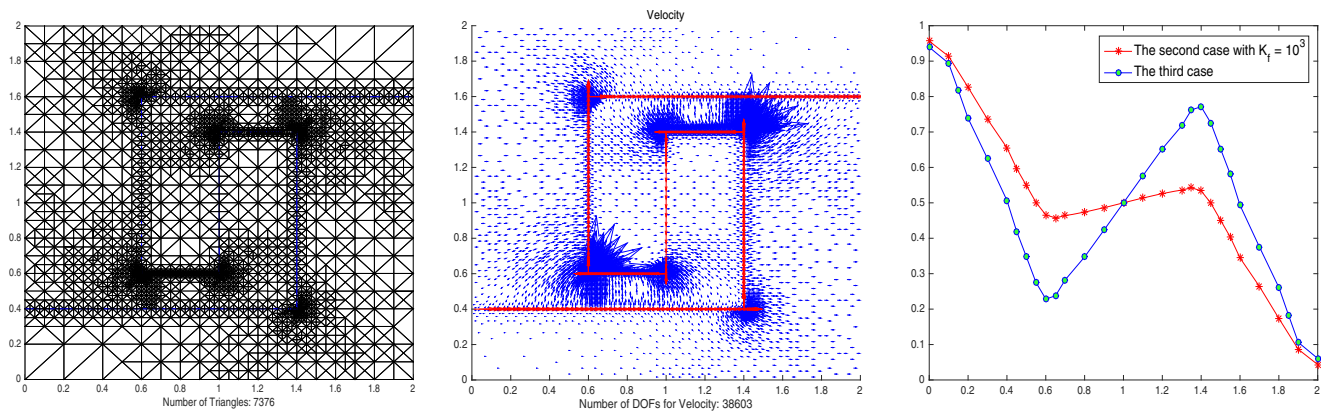


Figure 12. The third case of Example 5.2. (left) Adaptively refined mesh by adaptive mixed RT_1P_1 approximation. (Middle) The associated approximate velocity u_h^* . (right) Pressure profiles in matrix block along the line $y = 1$ for the second case with $K_f = 10^3$ and the third case.

We consider the third case for the reduced model (2) in the domain $\Omega = [0, 2] \times [0, 2]$ with a reduced fracture as in the second case. The boundary condition data and the permeability in the matrix block are the same as that in the second case, and the permeability in the fracture is shown in the right graph of Figure 7. We use the adaptive mixed RT_1P_1 approximation for this case. The left graph of Figure 12 displays the adaptively refined mesh. From the middle graph of Figure 12, we can also see that although the globally imposed pressure gradient tends to drive the fluid to the eastern direction, the fluid can flow backward to the western direction in the same local area as in the second case. The tend of flowing backward in the third case seems stronger than that in the second case, which is manifested by the pressure field distribution (see the right graph of Figure 12).

Example 5.3. In this example, we first consider the model (1) in the porous media with heterogeneous permeability $K = K \text{diag}(1, 1)$ as in the left graph of Figure 13. Then, we further consider the reduced model (2) in the same domain with a single fracture on the line $\{(x, y) : 0.8 \leq x \leq 2, y = 1\}$ which interacts with high-permeable and low-permeable zones. The permeability in the surrounding matrix block is also heterogeneous as the case without fracture, and the permeability in the fracture is $K_f = K_f \text{diag}(1, 1)$ where $K_f = 10^6$. For both cases, the boundary conditions in the matrix block are given as all the cases in Example 5.2. For the case with a single fracture, Dirichlet boundary condition holds on the fracture boundary as $\hat{p}_\gamma = 0$ at the end point $(2, 1)$, and homogeneous Neumann boundary condition is imposed at the interior end point $(0.8, 1)$. The adaptive mixed RT_1P_1 approximation is used for both cases. We apply the a posteriori error estimator introduced in Carstensen [1997] for the case without fracture.

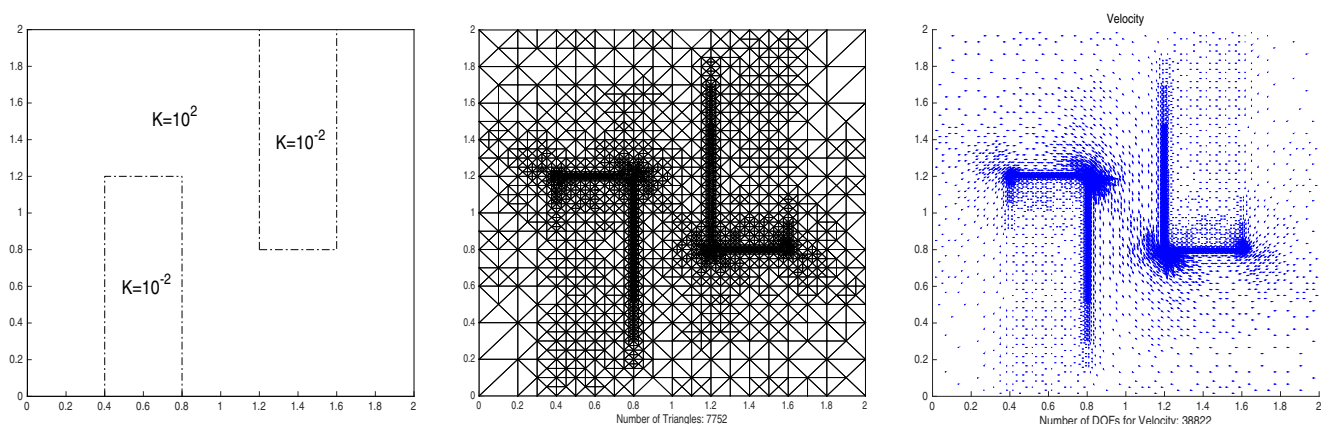


Figure 13. (left) The porous media, (middle) adaptively refined meshes, and (right) approximate velocity for the case without fracture.

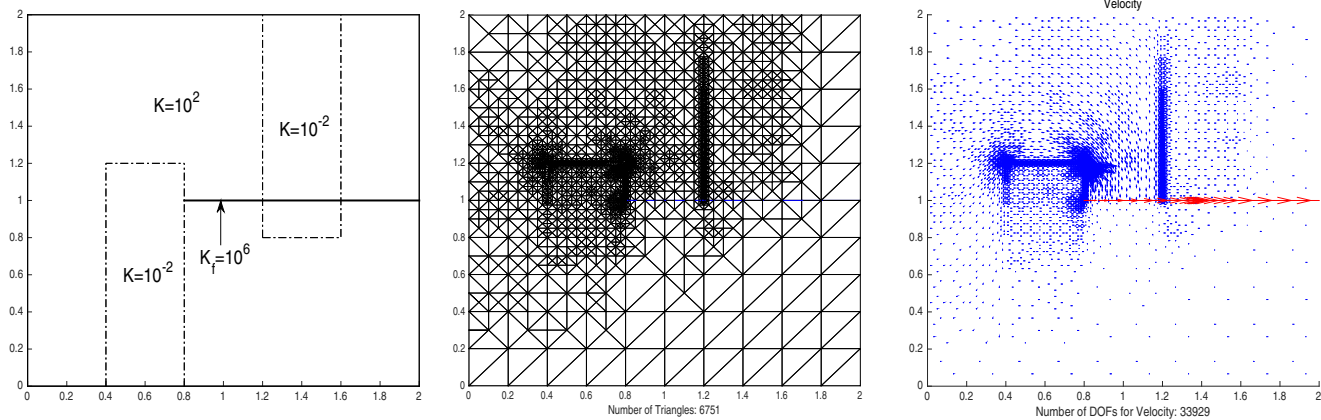


Figure 14. (left) The porous media, (middle) adaptively refined meshes, and (right) approximate velocity for the case with a single fracture.

The adaptively refined mesh and the approximate velocity are shown in the middle and right graphs of Figures 13 and 14 for the two cases, respectively. We can observe that when there is no fracture in the porous media, the fluid flows around the low-permeable zones to the outflow boundary. However, if there is a much higher-permeable fracture which interacts with high-permeable and low-permeable matrix blocks, then the fluid mainly tends to flow through the fracture to the outflow boundary. The second case shows how the fracture collects most of the flow within the matrix block and conducts it toward the outflow boundary.

Example 5.4. In this example, we consider the problem with a number of fractures which have fixed positions and lengths in a square porous media $\Omega=[0, 20] \times [0, 20]$ with permeability $\mathbf{K}=\text{diag}(1, 1)$ in the matrix and $\mathbf{K}_f=K_f \text{diag}(1, 1)$ in the fractures (see Figure 15). However, the fracture collection satisfies a certain distribution. First, we assume the fracture permeability is fixed as $K_f=10^5$ and consider that the fracture thickness satisfies $d=0.01d^*$, where d^* is a constant on a reduced fracture $\gamma_k|_{k=1,\dots,16}$ and satisfies the standard lognormal distribution with probability density function $f(x; \mu, \sigma) = \frac{1}{x\sigma\sqrt{2\pi}} \exp(-\frac{(\ln x - \mu)^2}{2\sigma^2})$. The boundary condition is assumed to be type of open-side boundary condition with $p=1$ on $x=0$, $p=0$ on $x=20$, and homogeneous Neumann boundary conditions are imposed at all the interior end points of fractures. We find that when μ is fixed, for instance, $\mu=1$, and $\sigma \in [0.01, 1]$ or when σ is fixed as $\sigma=1$, and $\mu \in [0.01, 1]$, different choice of parameter pair has weak influence on the solution of the problem. Here (μ, σ) are chosen such that $d^* \approx O(1)$ is not large.

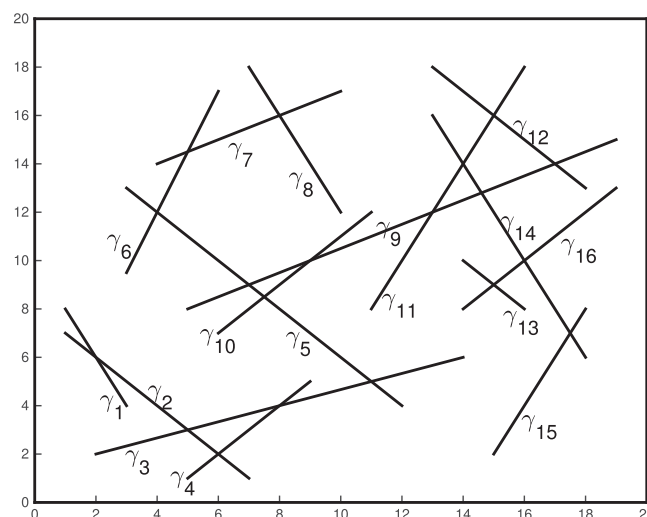


Figure 15. The matrix block and reduced fractures for Example 5.4.

We next consider the case by assuming the fracture permeability $K_f=10^5 K_f^*$ and K_f^* satisfies the standard lognormal distribution. We test the permeability distribution with $\sigma=1$, $\mu \in [1, 10]$ and $\mu=1$, $\sigma \in [1, 10]$. Figure 16 shows three cases of matrix pressure distribution for the problem with $\mu=1$, $\sigma=2, 4, 10$. For the problem with $\sigma=1$, $\mu \in [1, 10]$, the matrix pressure distribution is similar to the first two graphs of Figure 16. We find that for such extent, the choice of σ has more influence on the solution than μ .

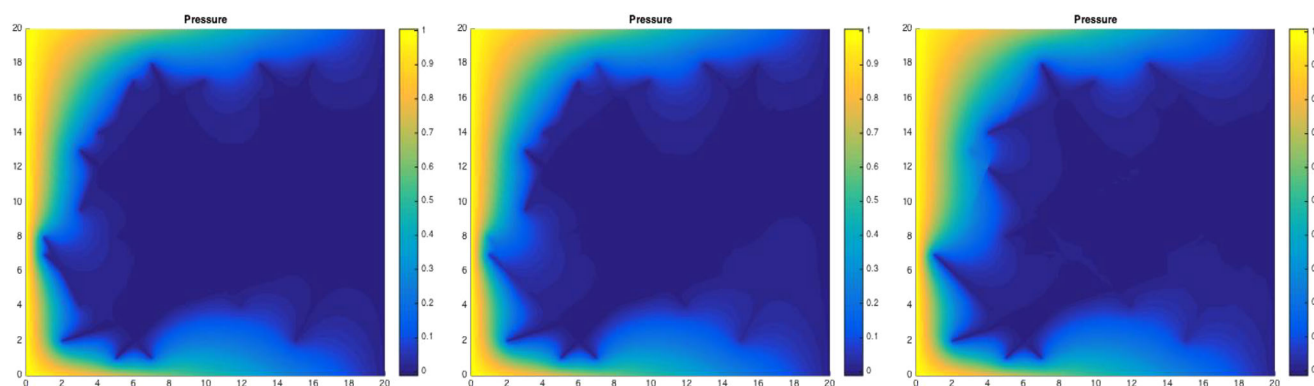


Figure 16. Matrix pressure distribution according to different lognormal distribution of permeability in fractures. (Left) $(\mu, \sigma) = (1, 2)$; (middle) $(\mu, \sigma) = (1, 4)$; (right) $(\mu, \sigma) = (1, 10)$.

6. Conclusion

The discrete fracture model, in which the fractures are dealt as a lower dimensional problem, is used in this paper as a reduced model framework for the simulation of single-phase Darcy flow in fractured porous media. We develop a robust adaptive mixed finite element method for the numerical solution of the reduced model. The key contribution of this work is to apply the adaptive mixed finite element method based on the residual-based a posteriori error estimators to simulate the flows which may have singularity in local subdomain. Another contribution of this work is to develop an efficient upscaling algorithm to compute the effective permeability in fractured porous media which can test the effects of fractures in a larger scale. We carefully design and compare a number of benchmark examples for computation of effective permeability of fractured porous media, and we make observation of some other interesting effects caused by fractures. A future work of interest is to extend the adaptive mixed finite element method for simulation of the reduced model in three-dimensional fractured porous media.

Acknowledgments

The authors would like to thank the anonymous reviewers for their insightful comments and suggestions that have contributed to improve this paper. No data were used in producing this manuscript, except in the fourth case of Example 5.1, where the data from the 10th SPE Comparative Solution Project on Upscaling (available at <http://www.spe.org/web/csp/>) were used. The work of H. Chen was supported by the NSF of China (grant 11201394) and the Fundamental Research Funds for the Central Universities (grant 20720150005). The work of S. Sun was supported by King Abdullah University of Science and Technology (KAUST) through the grant BAS/1/1351-01-01.

References

- Adams, R. (1975), *Sobolev Spaces*, Academic, N. Y.
- Alboin, C., J. Jaffré, J. E. Roberts, and C. Serres (2002), Modeling fractures as interfaces for flow and transport in porous media, in *Fluid Flow and Transport in Porous Media: Mathematical and Numerical Treatment, Contemporary Math.*, vol. 295, pp. 13–24, Springer-Verlag, Heidelberg.
- Baca, R., R. Arnett, and D. Langford (1984), Modeling fluid flow in fractured porous rock masses by finite element techniques, *Int. J. Numer. Methods Fluids*, 4, 337–348.
- Barenblatt, G., Y. Zheltov, and I. Kochina (1960), Basic concepts in the theory of seepage of homogeneous fluids in fissurized rocks, *J. Appl. Math. Mech.*, 24, 1286–1303.
- Brezzi, F., and M. Fortin (1991), *Mixed and Hybrid Finite Element Methods*, Springer, New York.
- Cai, J., and S. Sun (2013), Fractal analysis of fracture increasing spontaneous imbibition in porous media saturated with gas, *Int. J. Modern Phys. C*, 24(8), 1350056 (13 pages).
- Carstensen, C. (1997), A posteriori error estimate for the mixed finite element method, *Math. Comput.*, 66, 465–476.
- Carstensen, C., and R. H. W. Hoppe (2006), Error reduction and convergence for an adaptive mixed finite element method, *Math. Comput.*, 75, 1033–1042.
- Chen, L., M. Holst, and J. Xu (2010), Convergence and optimality of adaptive mixed finite element methods, *Math. Comput.*, 78, 35–53.
- D’Angelo, C., and A. Scotti (2012), A mixed finite element method for Darcy flow in fractured porous media with non-matching grids, *ESAIM Math. Modell. Numer. Anal.*, 46, 465–489.
- Dawson, C., S. Sun, and M. F. Wheeler (2004), Compatible algorithms for coupled flow and transport, *Comput. Methods Appl. Mech. Eng.*, 193, 2565–2580.
- Dong, C., S. Sun, and G. A. Taylor (2011), Numerical modeling of contaminant transport in fractured porous media using mixed finite element and finite volume methods, *J. Porous Media*, 14(3), 219–242.
- Du, S. H., S. Y. Sun, and X. P. Xie (2016), Residual-based a posteriori error estimation for multipoint flux mixed finite element methods, *Numer. Math.*, 134, 197–222.
- Durlofsky, L. J. (1991), Numerical calculation of equivalent grid block permeability tensors for heterogeneous porous media, *Water Resour. Res.*, 27, 699–708.
- Efendiev, Y., S. Lee, G. Li, J. Yao, and N. Zhang (2015), Hierarchical multiscale modeling for flows in fractured media using generalized multi-scale finite element method, *Int. J. Geomath.*, 6, 141–162.
- Ervin, V. J., E. W. Jenkins, and S. Sun (2009), Coupled generalized non-linear Stokes flow with flow through a porous medium, *SIAM J. Numer. Anal.*, 47(2), 929–952.
- Formaggia, L., A. Fumagalli, A. Scotti, and P. Ruffo (2014), A reduced model for Darcy’s problem in networks of fractures, *ESAIM Math. Modell. Numer. Anal.*, 48, 1089–1116.
- Frih, N., J. E. Roberts, and A. Saada (2008), Modeling fractures as interfaces: A model for Forchheimer fractures, *Comput. Geosci.*, 12, 91–104.

- Fumagalli, A. (2012), Numerical modelling of flows in fractured porous media by the XFEM method, PhD thesis, Politecnico di Milano, Milan, Italy.
- Hajibeygi, H., D. Karvounis, and P. Jenny (2011), A hierarchical fracture model for the iterative multiscale finite volume method, *J. Comput. Phys.*, **230**, 8729–8743.
- Hoteit, H., and A. Firoozabadi (2005), Multicomponent fluid flow by discontinuous Galerkin and mixed methods in unfractured and fractured media, *Water Resour. Res.*, **41**, W11412, doi:10.1029/2005WR004339.
- Hoteit, H., and A. Firoozabadi (2008), An efficient numerical model for incompressible two-phase flow in fractured media, *Adv. Water Resour.*, **31**, 891–905.
- Karimi-Fard, M., and L. J. Durlofsky (2014), Unstructured adaptive mesh refinement for flow in heterogeneous porous media, paper presented at 14th European Conference on the Mathematics of Oil Recovery, ECMOR XIV and Catania, Sicily, Italy.
- Karimi-Fard, M., B. Gong, and L. J. Durlofsky (2006), Generation of coarse-scale continuum flow models from detailed fracture characterizations, *Water Resour. Res.*, **42**, W10423, doi:10.1029/2006WR005015.
- Larson, M. G., and A. Maqvist (2008), A posteriori error estimates for mixed finite element approximations of elliptic problems, *Numer. Math.*, **108**, 487–500.
- Lee, S. H., C. L. Jensen, and M. F. Lough (2000), Efficient finite-difference model for flow in a reservoir with multiple length-scale fractures, *SPE J.*, **3** (5), 268–275.
- Lee, S. H., M. F. Lough, and C. L. Jensen (2001), Hierarchical modeling of flow in naturally fractured formations with multiple length scales, *Water Resour. Res.*, **37**, 443–455.
- Li, L., and S. H. Lee (2008), Efficient field-scale simulation of black oil in naturally fractured reservoir through discrete fracture networks and homogenized media, *SPE Reserv. Eval. Eng.*, **11**, 750–758.
- Lough, M. F., S. H. Lee, and J. Kamath (1997), A new method to calculate effective permeability of gridblocks used in the simulation of naturally fractured reservoirs, *SPE Reserv. Eng.*, **12**, 219–224.
- Lovadina, C., and R. Stenberg (2006), Energy norm a posteriori error estimates for mixed finite element methods, *Math. Comput.*, **75**, 1659–1674.
- Martin, V., J. Jaffré, and J. E. Roberts (2005), Modeling fractures and barriers as interfaces for flow in porous media, *SIAM J. Sci. Comput.*, **26**, 1667–1691.
- Moinfar, A., W. Narr, R. Hui, B. Mallison, and S. H. Lee (2011), Comparison of discrete-fracture and dual-permeability models for multiphase flow in naturally fractured reservoirs, paper SPE 142295 presented at SPE Reservoir Simulation Symposium, Soc. of Pet. Eng., The Woodlands, Tex., 21–23 Feb.
- Moortgat, J., S. Sun, and A. Firoozabadi (2011), Compositional modeling of three-phase flow with gravity using higher-order finite element methods, *Water Resour. Res.*, **47**, W05511, doi:10.1029/2010WR009801.
- Nakashima, T., N. Arihara, and S. Sutopo (2001), Effective permeability estimation for modeling naturally fractured reservoirs, paper SPE 68124 presented at SPE Middle East Oil Show, Soc. of Pet. Eng., Manama.
- Noorishad, J., and M. Mehran (1982), An upstream finite element method for solution of transient transport equation in fractured porous media, *Water Resour. Res.*, **18**, 588–596.
- Oda, M. (1985), Permeability tensor for discontinuous rock masses, *Geotechnique*, **35**, 438–495.
- Pruess, K., and T. Narasimhan (1985), A practical method for modeling fluid and heat flow in fractured porous media, *SPE J.*, **25**, 14–26.
- Schwenck, N. (2015), An XFEM-based model for fluid flow in fractured porous media, PhD thesis, Univ. of Stuttgart, Dep. of Hydromech. and Modell. of Hydrosyst., Stuttgart, Germany.
- Song, P., and S. Sun (2012), Contaminant flow and transport simulation in cracked porous media using locally conservative schemes, *Adv. Appl. Math. Mech.*, **4**(4), 389–421.
- Sun, S., and M. F. Wheeler (2005), Symmetric and nonsymmetric discontinuous galerkin methods for reactive transport in porous media, *SIAM J. Numer. Anal.*, **43**(1), 195–219.
- Sun, S., and M. F. Wheeler (2006), Anisotropic and dynamic mesh adaptation for discontinuous Galerkin methods applied to reactive transport, *Comput. Methods Appl. Mech. Eng.*, **195**(25–28), 3382–3405.
- Sun, S., and M. F. Wheeler (2007), Discontinuous Galerkin methods for simulating bioreactive transport of viruses in porous media, *Adv. Water Resour.*, **30**(6–7), 1696–1710.
- Warren, J., and P. Root (1963), The behavior of naturally fractured reservoirs, *SPE J.*, **3**, 245–255.
- Wen, X. H., and J. J. Gomez-Hernandez (1996), Upscaling hydraulic conductivities in heterogeneous media, *J. Hydrol.*, **183**, 9–32.
- Wu, X. H., Y. Efendiev, and T. Y. Hou (2002), Analysis of upscaling absolute permeability, *Discrete Continuous Dyn. Syst., Ser. B*, **2**, 185–204.
- Wu, Y. S., and K. Pruess (1988), A multiple-porosity method for simulation of naturally fractured petroleum reservoirs, *SPE Reserv. Eng.*, **3**, 327–336.
- Zhang, D. (2002), *Stochastic Methods for Flow in Porous Media: Coping With Uncertainties*, Academic Press, San Diego, Calif.
- Zidane, A., and A. Firoozabadi (2014), An efficient numerical model for multicomponent compressible flow in fractured porous media, *Adv. Water Resour.*, **74**, 127–147.